FEATURE ARTICLE

Kinetic Study of Heterogeneous Reaction of Deliquesced NaCl Particles with Gaseous HNO_3 Using Particle-on-Substrate Stagnation Flow Reactor Approach

Y. Liu,[†] J. P. Cain,[‡] H. Wang,*[,‡] and A. Laskin*[,†]

William R. Wiley Environmental Molecular Sciences Laboratory, Pacific Northwest National Laboratory, P. O. Box 999, MSIN K8-88, Richland, Washington 99352, and Department of Aerospace and Mechanical Engineering, University of Southern California, Los Angeles, California 90089-1453

Received: March 12, 2007; In Final Form: June 12, 2007

Heterogeneous reaction kinetics of gaseous nitric acid with deliquesced sodium chloride particles NaCl(aq) + HNO_3(g) → $NaNO_3$(aq) + HCl(g) were investigated with a novel particle-on-substrate stagnation flow reactor (PS-SFR) approach under conditions, including particle size, relative humidity, and reaction time, directly relevant to the atmospheric chemistry of sea salt particles. Particles deposited onto an electron microscopy grid substrate were exposed to the reacting gas at atmospheric pressure and room temperature by impingement via a stagnation flow inside the reactor. The reactor design and choice of flow parameters were guided by computational fluid dynamics to ensure uniformity of the diffusion flux to all particles undergoing reaction. The reaction kinetics was followed by observing chloride depletion in the particles by computer-controlled scanning electron microscopy with energy-dispersive X-ray analysis (CCSEM/EDX). The validity of the current approach was examined first by conducting experiments with median dry particle diameter $\bar{D}_p = 0.82$ μm, 80% relative humidity, particle loading densities $4 \times 10^4 \leq N_s \leq 7 \times 10^6$ cm^{-2} and free stream HNO_3 concentrations 2, 7, and 22 ppb. Upon deliquescence the droplet diameter $\bar{D}_d$ approximately doubles. The apparent, pseudo-first-order rate constant determined in these experiments varied with particle loading and HNO_3 concentration in a manner consistent with a diffusion-kinetic analysis reported earlier (Laskin, A.; Wang, H.; Robertson, W. H.; Cowin, J. P.; Ezell, M. J.; Finlayson-Pitts, B. J. *J. Phys. Chem. A* **2006**, *110*, 10619). The intrinsic, second-order rate constant was obtained as $k_{II} = 5.7 \times 10^{-15}$ cm^3 molecule^{-1} s^{-1} in the limit of zero particle loading and by assuming that the substrate is inert to HNO_3. Under this loading condition the experimental, net reaction uptake coefficient was found to be $\gamma_{net} = 0.11$ with an uncertainty factor of 3. Additional experiments examined the variations of HNO_3 uptake on pure NaCl, a sea salt-like mixture of NaCl and $MgCl_2$ (Mg-to-Cl molar ratio of 0.114) and real sea salt particles as a function of relative humidity. Results show behavior of the uptake coefficient to be similar for all three types of salt particles with $\bar{D}_p \sim 0.9$ μm over the relative humidity range 20−80%. Gaseous HNO_3 uptake coefficient peaks around a relative humidity of 55%, with γ_{net} well over 0.2 for sea salt. Below the efflorescence relative humidity the uptake coefficient declines with decreasing RH for all three sea salt types, and it does so without exhibiting a sudden shutoff of reactivity. The uptake of HNO_3 on sea salt particles was more rapid than that on the mixture of NaCl and $MgCl_2$, and uptake on both sea salt and sea salt-like mixture was faster than on pure NaCl. The uptake of HNO_3 on deliquesced, pure NaCl particles was also examined over the particle size range of $0.57 \leq \bar{D}_p \leq 1.7$ μm ($1.1 \leq \bar{D}_d \leq 3.4$ μm) under a constant relative humidity of 80%. The uptake coefficient decreases monotonically with an increase in particle size. Application of a resistance model of reaction kinetics and reactant diffusion over a single particle suggests that, over the range of particle size studied, the uptake is largely controlled by gaseous reactant diffusion from the free stream to the particle surface. In addition, a combined consideration of uptake coefficients obtained in the present study and those previously reported for substantially smaller droplets ($\bar{D}_d \sim 0.1$ μm) (Saul, T. D.; Tolocka, M. P.; Johnston, M. V. *J. Phys. Chem. A* **2006**, *110*, 7614) suggests that the peak reactivity occurs at a droplet diameter of ∼0.7 μm, which is immediately below the size at which sea salt aerosols begin to notably contribute to light scattering.

Introduction

Over the last few decades a great deal of attention has been placed on the fundamental kinetics and mechanism of atmospheric heterogeneous reactions. Reactions involving aerosol are known to impact atmospheric composition and chemistry,[1−8] global radiative forcing and climate change,[9−15] sky visibility[16,17] and public health.[18−22] Sea salt aerosols, generated by wind-induced wave action and bubble bursting of seawater, are the second largest component (by mass) of global aerosol burden.[23] These aerosols may undergo heterogeneous reactions with trace species in the atmosphere, including OH,

* Authors to whom correspondence should be addressed. H.W.: e-mail, haiw@usc.edu; phone, (213) 740-0499; fax, (213) 740-8071. A.L.: e-mail, Alexander.Laskin@pnl.gov; phone, (509) 376-8741; fax, (509) 376-6066.
[†] Pacific Northwest National Laboratory.
[‡] University of Southern California.

10.1021/jp072005p CCC: $37.00
Published on Web 09/13/2007

Yong Liu received his B.S. degree in Applied Chemistry, 1997, from Fudan University in Shanghai, China. He did his graduate studies at Fudan University (M.S., 2000) with Professor Xiaoyin Chen and then at University of Michigan, Ann Arbor (Ph.D., 2005) under the direction of Professor John R. Barker. Currently, he is a postdoctoral research associate at the William R. Wiley Environmental Molecular Sciences Laboratory at the Pacific Northwest National Laboratory with Dr. Alexander Laskin. His research interests include heterogeneous atmospheric chemistry, aerosol science and its applications to climate and atmospheric chemistry, and environmental catalysis.

Jeremy Cain received a B.S. in Mechanical Engineering from the University of Tulsa in 2003. He then began graduate studies in the same discipline at the University of Illinois—Urbana, Champaign. His research there was on the radiant ignition of solid rocket composite propellant. Upon completion of his Master's degree in 2005, he moved to the University of Southern Californian to pursue a Ph.D study under the direction of Professor Hai Wang. His research interests include gas-phase and heterogeneous chemical kinetics, computational fluid dynamics and reacting flow simulations, and quantum chemistry modeling of reaction kinetics.

HNO_3, O_3, NO_2, N_2O_5, and $ClONO_2$. The net result is that inert halides may be converted to a variety of photochemically reactive halogen species,[1−3,5,10,24−59] which lead to production of reactive halogen species $X^\bullet$ and $XO^\bullet$ (X = Cl and Br) upon exposure to sunlight. There has been increasing evidence from laboratory and field studies that these halogen atoms play pivotal roles in the chemistry of the marine boundary layer.[27,60−66] For these reasons a quantitative understanding of the uptake and kinetics of reactive gases on sea salt particles is critical toward elucidating the overall halogen budget and tropospheric chemistry.

The reaction of NaCl with gaseous HNO_3 has garnered great recognition over the last two decades. Considerable work[3,35,43−45,50,52,53,55,67−73] has been directed toward the uptake mechanism and rate of HNO_3 onto NaCl:

Hai Wang received his Ph.D. in Fuel Science in 1992 from Penn State. His graduate research under the guidance of Professor Michael Frenklach included development of a fundamental kinetic model of soot formation, application of quantum chemistry and reaction rate theories in high-temperature kinetics of aromatics, theories and applications of chemical vapor deposition of diamond thin films, and chemistry in the interstellar media. He was also involved in the development of the earlier versions of the GRI Mech. He was a Professional Research Staff at Princeton University from 1994 to 1996, working under the supervision of Professor Ed Law. During that period of time, his research included fundamental chemical kinetics of hydrocarbon combustion and laminar flames. In 1997, he joined the faculty of Mechanical Engineering at the University of Delaware, and continued his studies of hydrocarbon reaction kinetics at high temperatures. Currently he is a Professor of Aerospace and Mechanical Engineering at the University of Southern California. His recent research activities include the application of quantum chemistry and statistical mechanical theories in gas-phase and gas-surface chemical kinetics, transport properties of reacting gases, and theory of molecular and nanoparticle transport. His other research activities include combustion generated particulates, atmospheric heterogeneous reaction kinetics, catalysis, nanomaterial synthesis and characterization, and semiconductor metal oxides for chemical sensor and solar energy conversion applications. He has published over 100 articles. He was the recipient of the National Science Foundation Career Award in 1999 and the Distinguished Paper Award from the Combustion Institute in 2006.

Alexander Laskin received his Ph.D. degree in 1998 from the Hebrew University of Jerusalem, Israel. His graduate research under the guidance of Professor Assa Lifshitz included studies of the kinetics and the chemical reaction mechanisms of high temperature pyrolysis of aromatic compounds. During a one-year postdoctoral appointment in 1999 at the University of Delaware and Princeton University (joint position) with Professors H. Wang and C. K. Law his research was focused on development of comprehensive kinetic models for combustion of hydrocarbon fuels. In 1999, Dr. Laskin joined the staff of the Pacific Northwest National Laboratory (PNNL) as a post-doctoral researcher where he began research focused on the chemistry of atmospheric aerosols. Currently he is a Senior Research Scientist at the William R. Wiley Environmental Molecular Sciences Laboratory of PNNL. His present and past research interests include the following: environmental impact of aerosols; physical chemistry of gas-particle interactions; novel methods of aerosol collection and measurement; single-particle analysis of aerosols; source apportionment of aerosols; combustion related aerosols; combustion chemistry and chemical kinetics. He has authored and co-authored over 40 articles.

$$NaCl(s,aq) + HNO_3(g) \rightarrow NaNO_3(aq) + HCl(g) \quad (1)$$

The above acid replacement reaction releases HCl into the gas phase and causes nitrate enrichment, leading to halide deficiency in sea salt aerosols. In clean air where reactive species are absent, HCl is quite stable because of its negligible cross section for absorption of light with wavelength above 290 nm.[74] Upon entrainment into polluted air, however, HCl can undergo reaction with •OH to generate a highly reactive Cl• atom and ultimately form photochemically labile Cl_2 and HOCl, as shown in Figure 1. The generation of Cl• atoms in the lower atmosphere can result in either ozone depletion or ozone formation, depending on atmospheric conditions.[74,75] Furthermore, reaction 1 is also one of the most prevalent pathways for sea salt aging in the atmosphere.

Sea salt aerosol can be entrained in atmospheric air and transported over hundreds of miles. They are eventually removed from the air by dry or wet deposition, but this process may take anywhere from days to weeks to occur. The physicochemical properties of sea salts can be altered considerably during this transportation process. Reaction 1 leads to the formation of nitrate salt particles that are more hygroscopic than NaCl and do not readily crystallize. It also is known that the properties of NaCl mixed with nitrate salt, including size, phase, water content, and optical reflection and scattering, respond to humidity much differently than those of pure NaCl. For example, the presence of nitrate causes NaCl to attain a liquid phase near or at its defects, steps and edges of the droplet surface, and the reaction rate of NaCl in aqueous phase is known to be much faster than that in solid phase.[44] Thus, the variations of these properties may impact aerosol chemical reactivity and its effect on climate, both directly (absorption and scattering of light) and indirectly (cloud condensation nucleation activity).[74,75]

The kinetics of reaction 1 have been studied extensively.[3,35,43−45,50,52,53,55,67−73] Despite being a rather simple reaction, the reaction rate and its dependency on particle size and relative humidity remain highly uncertain. For example, the value reported for reactive fraction of collisions, i.e., the uptake coefficient for reaction 1, spans several orders of magnitude. References to a comprehensive account of those studies can be found in a number of recent publications.[3,5,55,74] The large discrepancy found in reactive uptake is generally believed to stem from different amounts of water absorbed on the salt surface.[52] Water absorption usually occurs at or near surface defects, steps and edges, and the extent of absorption clearly depends on humidity.

Particles in the marine boundary layer are routinely exposed to moist air with relative humidity (RH) > 75%.[76,77] Most previous studies were conducted on NaCl crystals or powders in vacuum or in dry air below the efflorescence relative humidity (ERH) of NaCl (~45%). Earlier Knudsen cell and some flow reactor experiments were very instrumental to elucidating the fundamental mechanism of reaction 1, but they are of indirect relevance to atmospheric chemistry because of the near vacuum conditions employed in those studies. To date there are very limited data available for HNO_3(g) uptake onto deliquesced NaCl or sea salt particles under conditions directly relevant to atmospheric chemistry of sea salt aerosols. Table 1 summarizes the reaction probabilities recently reported for HNO_3(g) with deliquesced NaCl and sea salt particles (droplets). Johnston and co-workers[52,53] observed the reaction kinetics and uptake in a flow reactor for both NaCl and a mixture of NaCl and $MgCl_2$ over a droplet diameter range 0.1−0.23 μm and relative humidity range 10−85%. They reported uptake coefficient

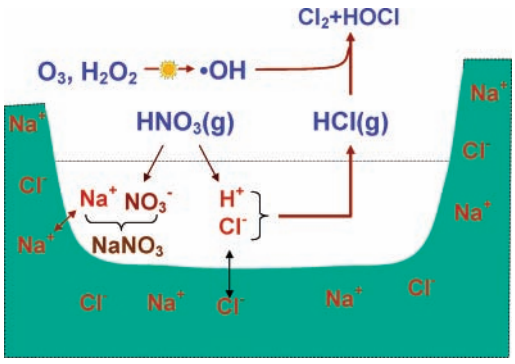

Figure 1. Heterogeneous reactions occurring in the marine boundary layer: uptake of HNO_3 onto NaCl and reaction of its product, HCl, with OH.[55] Copyright 2000, American Chemical Society.

values substantially smaller, by more than an order of magnitude, than that of an earlier study conducted for smaller droplets under a relative humidity of 55%.[51] Only one study has been reported[45] for droplet size larger than 1 μm.

The purposes of the present study are to conduct a systematic investigation of the kinetics of reaction 1 and to experimentally determine the influences of particle size and humidity on the uptake coefficient of HNO_3(g) on NaCl. In addition, the uptake on a sea salt-like mixture of NaCl and $MgCl_2$ and sea salt particles was examined in detail. The experiments were carried out under conditions comparable to that of the ambient atmosphere using a novel particle-on-substrate stagnation flow reactor (PS-SFR) experimental approach. The PS-SFR approach has emerged from a number of recent experimental developments and studies of gas-to-particle heterogeneous chemistry of aerosols.[78−86] In those studies, exposures of substrate-deposited particles to hydroxyl (OH) radicals, ozone (O_3), nitric acid (HNO_3), water vapor, and UV light were made and the influence of particle composition, structure, and morphology on the reaction mechanisms and relative rates in dry and moist air were elucidated. In our most recent study[86] of the reaction kinetics for gaseous hydroxyl radicals (OH) with deliquesced sodium chloride particles, we demonstrated that fundamental reaction kinetics data may be obtained from this type of experiment after a quantitative analysis of the effects of gaseous reactant transport from the bulk gas to the substrate surface. Such effects arise from the close proximity of the reacting particles mounted on the substrate. In that study the reaction kinetics of substrate-deposited, micron-size NaCl particles was examined using an automated X-ray microanalysis of the chemical composition of individual particles following their exposure to hydroxyl radicals. This manuscript presents a new design of the experimental apparatus, in which the reactor geometry and choice of flow parameters were guided by computational fluid dynamics to ensure uniformity of the diffusion flux to all particles undergoing reaction. The utility of the experimental protocol and data interpretation is then demonstrated using a case kinetic study of HNO_3-to-NaCl heterogeneous reaction.

Uptake of $HNO_{3(g)}$ on deliquesced NaCl particles was recently carefully examined by Johnston and co-workers[52,53] using a flow reactor coupled to a single particle mass spectrometer (FR-SPMS). The particle diameter ranged from 0.1 to 0.23 μm in their studies. In the present study we carried out a systematic investigation of the heterogeneous reaction kinetics for deliquesced NaCl particles 1−3.4 μm in diameter using the PS-SFR approach in combination with the CCSEM/EDX particle analysis. We determined the reactive uptake of HNO_3 as a function of relative humidity (20−80%) for NaCl, a

TABLE 1: Reactive Uptake Coefficients Reported for HNO_3(g) onto Deliquesced NaCl and Sea Salt Particles at Room Temperature

type of salt	experimental technique	droplet diameter, D_d (μm)	[HNO_3] (ppb)	RH (%)	exposure time, t (s)	uptake coefficient, γ_{net}	ref
NaCl	FR-CIMS[a]	2−4	∼370−740	75	6	>0.2	45
sea salt	FR-N^{13} isotope tracer	∼0.07	2−575	55	0.2−2	0.5 ± 0.2	51
NaCl	FR-SPMS[b]	0.11−0.22	60−380	80	31	0.0049−0.012[d]	52
NaCl and NaCl/$MgCl_2$	FR-SPMS	0.10−0.233	60	10−85	<10	0.023−0.126[d]	53
NaCl, NaCl/$MgCl_2$, and sea SALT	PS-SFR CCSEM/EDX[c]	1.1−3.4	∼2−20	20−80	600−43200	0.026−0.2[d]	this work

[a] Flow reactor−chemical ionization mass spectrometer. [b] Flow reactor−single particle mass spectrometer. [c] Particles-on-substrate stagnation flow reactor−computer-controlled scanning electron microscopy with energy-dispersed analysis of X-ray. [d] Variation of the uptake coefficient is due to RH, droplet size, and composition variation.

mixture of NaCl/$MgCl_2$ characteristic of sea salt ($X_{Mg/Na}$ = 0.114) and sea salt particles. Measurements yielded a net uptake coefficient γ_{net} = 0.11 (× 2.9/÷2.8) under RH = 80% for deliquesced NaCl droplets roughly 1.6 μm in diameter. The influences of particle size and relative humidity on the uptake coefficient were also determined. Results from the present work offer much needed kinetic data for atmospheric modeling and insight into the humidity and particle size dependencies of reactive uptake.

Experimental Section

Materials and Sample Preparation. Nearly monodisperse NaCl particles were generated from an aqueous 0.5 M solution of NaCl (Aldrich, Inc., 99.99% purity) using a home-built nebulizer. The particles were dried in a diffusion drier (TSI, Inc., model 3062) prior to sizing and substrate deposition with a micro-orifice uniform deposit impactor (MOUDI) (MSP, Inc., model 110). Most experiments used stage 5 of the MOUDI to collect dry particles approximately 0.8 μm in diameter, which were deposited onto TEM grids (Formvar supported Carbon film, 400 mesh nickel grids, Electron Microscopy Sciences, Inc.) mounted on an appropriate impaction plate. The size uniformity of deposited particles was confirmed by computer-controlled scanning electron microscopy (CCSEM) analysis of over 3000 particles on several different grids. Figure 2 shows an SEM image of a typical particle sample and its size distribution measured from the equivalent circle diameter based on two-dimensional projected area of the particles. In this particular case the size distribution is log-normal with a median diameter $\bar{D}_p$ = 0.80 μm and geometric standard deviation σ = 1.2.

Particle Exposure Apparatus. A schematic of the experimental reactor is shown in Figure 3. The reactor design was based on a laminar jet of HNO_3, highly diluted with moist nitrogen, impinging onto a substrate-deposited sample. Principles of fluid mechanics state that the axial convective velocity is zero immediately above the surface; the transport of gaseous reacting species to particle surfaces is purely accomplished by molecular diffusion. The design was guided by computational fluid dynamics (CFD) simulations to ensure reliability of the kinetic measurements and to minimize systematic experimental error. These simulations are discussed in detail later. In each experiment one TEM grid loaded with NaCl particles of a known number density N_s is placed atop a cylindrical Teflon sample holder 1 in. in diameter. The sample and its holder were placed inside a sealed borosilicate glass chamber constructed from standard 75 mm joint with FETFE O-ring quick seal (Ace Glass, Inc., part number 7646-18). The TEM grid was fixed in place on the surface of the sample holder using a magnet embedded inside the holder.

The reactor and its gas delivery lines were built from glass and Teflon parts; neither material reacts with the HNO_3 vapor.

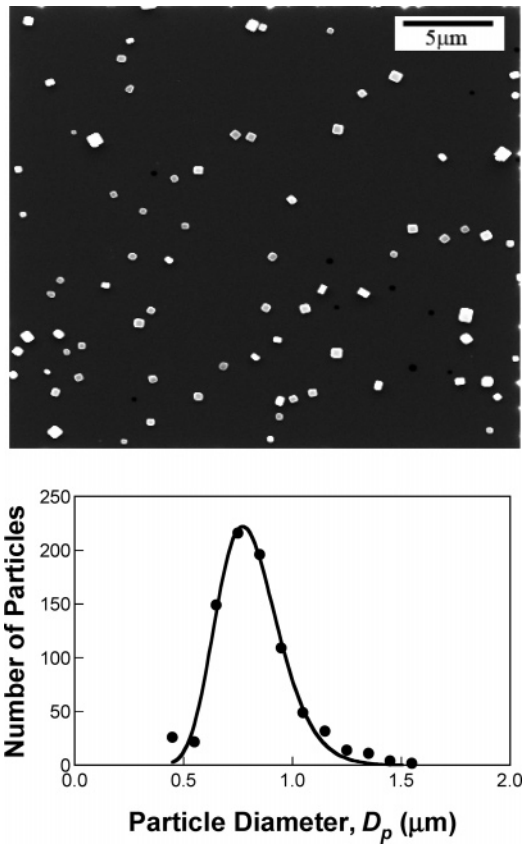

Figure 2. SEM image (top panel) and CCSEM measured particle size distribution (symbols in the bottom panel) of a typical NaCl sample. Size distribution may be fitted by a log-normal distribution (solid line).

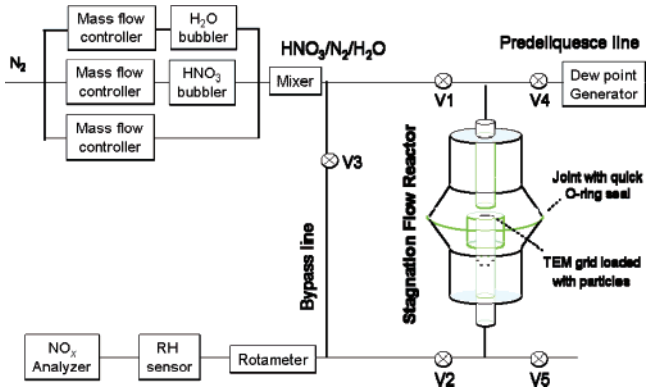

Figure 3. Schematic of the experimental setup.

Nitrogen was used as a carrier gas and allowed to flow through two bubblers containing concentrated HNO_3 solution and distilled water, respectively. Composition of the $HNO_3/H_2O/N_2$ mixture and its flow rate was controlled by three mass

controllers installed upstream of the reactor, as shown in Figure 3. Readings of the rotameter installed downstream of the reactor ensure no negative flow (into the apparatus) or leaks. A chemiluminescence NO_y analyzer (Thermo Electron, Inc., model 42C-Y) and an in-line relative humidity sensor (Honeywell, Inc., model HIH4000) were used to monitor HNO_3 concentration and RH, respectively. During each experiment, both measurements were made continuously and fluctuations were smaller than 5% and 1% in concentration and relative humidity, respectively.

The fact that HNO_3 can absorb on the reactor wall required some special considerations. At room temperature Teflon has less than 5% HNO_3 adsorption after minutes of HNO_3 exposure.[87] Glass can be passivated to HNO_3 adsorption after exposure for several hours. To ensure no significant loss of HNO_3 on the walls of the apparatus and its gas lines, the reactor was passivated before each experiment for at least 2 h with a flow of the $HNO_3/H_2O/N_2$ mixture. After a steady-state exposure condition was established, the TEM sample grid was installed by opening the reactor joint and then quickly sealing the joint with screwlock pinch clamps. During sample installation the desired HNO_3 concentration and RH level were perturbed, but they were recovered within 1 min. to the initially set values, as confirmed by stable HNO_3 concentration readouts during the course of the experiments. The period of perturbation was always substantially shorter than the total reaction time employed, which ranged from 8 to 300 min.

The HNO_3 passivation procedure was applied in all measurements made at 80% RH. Under other RH values, particles were first wetted by a moist airflow (RH = 80%) generated by a dew point generator (Li-Cor, Inc., model LI-610) for 2 min prior to switching on a gas stream with a preset RH and HNO_3 concentration.

In all studies the flow of gas with a controlled RH level and HNO_3 concentration is ejected at a rate of $V = 2$ L/min (STP) from a $^1/_2''$ diameter (outer) borosilicate glass tube (inner diameter $d = 0.8$ cm). The flow impinges upon particles deposited on a single TEM grid whose center is placed along the flow tube centerline. The distance between the tube exit and the grid surface is $L = 0.2$ cm ($L/d = {}^1/_4$). The experiments were conducted at ambient temperature and atmospheric pressure.

CCSEM/EDX Single-Particle Analysis. Computer-controlled scanning electron microscopy (CCSEM) coupled with energy-dispersed X-ray (EDX) spectrometry was used to determine the elemental composition and loading density of NaCl particles. The instrument used in this study is a FEI XL30 digital field emission gun environmental SEM. The microscope is equipped with an EDAX spectrometer (EDAX, Inc., model PV7761/54 ME) that has an Si(Li) detector 30 mm^2 in active area and an ATW2 window, which allows X-ray detection from elements higher than beryllium ($Z > 4$). The system is equipped with *Genesis* hardware and software (EDAX, Inc.) for computer-controlled SEM/EDX particle analysis. Particles were recognized by an increase in the detector signal above a threshold value. The program acquires an X-ray spectrum from each detected particle. Particle imaging[85] was made by acquiring the mixed signal of backscattered (BSE) and transmitted (TE) electrons. During the X-ray acquisition the electron beam scanned over the particle projection area. The X-ray spectra were acquired for 10 s at a beam current of ~500 pA and an accelerating voltage of 20 kV. These conditions are sufficient to collect ~2000 photon counts per Na and Cl characteristic peaks. For quantification of the EDX results, the *Genesis* software utilizes a standardless microanalysis method that relates X-ray intensities to elemental concentrations through theoretically calculated

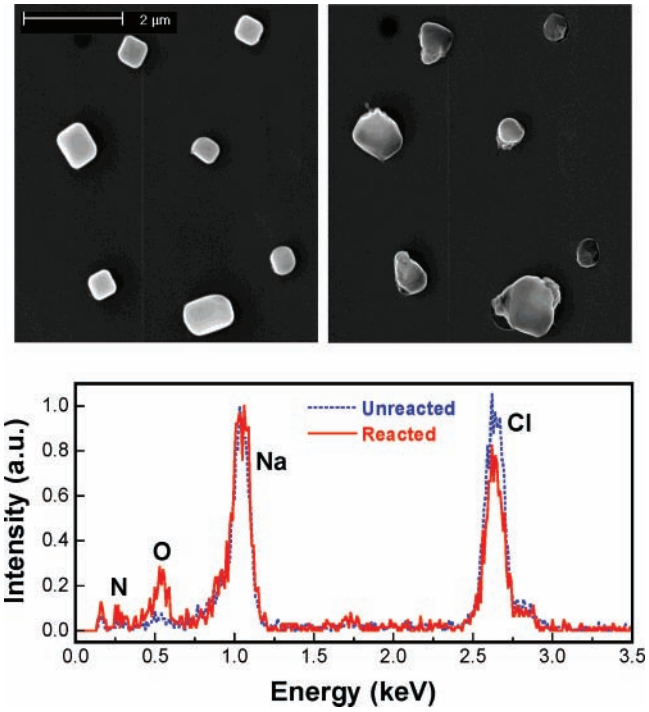

Figure 4. Top panels: SEM images of NaCl particles before (left) and after (right) reaction with gaseous HNO_3 of 6 ppb concentration, 80% RH and reaction time of 210 min. Bottom panel: typical EDX spectra of individual NaCl particle before and after reaction.

equivalent intensities of corresponding peaks. Details of the applied quantification method can be found elsewhere.[88]

Experimental Protocol. Although the particle exposure apparatus is quite different from that used in a previous study,[86] the experimental protocol is very similar. Briefly, a constant flow of mixed $HNO_3/H_2O/N_2$ gases impinges on NaCl deposited onto the grid to provide a uniform HNO_3 flux. The change in Cl-to-Na molar ratio ($[Cl/Na]_t^{EDX}$) of reacted particles was taken to quantify chloride loss from reaction 1, i.e.,

$$\frac{[Cl^-]_{d,t}}{[Cl^-]_{d,t=0}} = \frac{[Cl/Na]_t^{EDX}}{[Cl/Na]_{t=0}^{EDX}} \qquad (2)$$

where the subscript d denotes the NaCl droplet and t the reaction time. Figure 4 shows typical SEM images of NaCl particles before and after exposure to gaseous nitric acid. Morphological changes, indicative of reactive transformation, are clearly seen. Evidence of reaction occurrence is also demonstrated in the EDX spectra: comparison of the spectra before and after reaction, as shown in Figure 4, reveal a depletion of chlorine.

Three series of experiments were conducted. In series A the apparent, pseudo-first-order rate constant was measured and the uptake coefficient determined for HNO_3 reaction with deliquesced NaCl particles of diameter $\bar{D}_d = 1.6$ μm (median dry diameter $\bar{D}_p = 0.8$ μm) at 80% relative humidity. The measurement was made over a range of free stream HNO_3 concentrations (2, 7, and 22 ppb) similar to the 10−20 ppb level reported in polluted environments.[89] For each HNO_3 concentration a range of particle loadings ($N_s = 4 \times 10^4$ to 7×10^6 cm^{-2}) were used and reaction times were varied accordingly. More than 150 samples were tested and analyzed. A vast majority of the samples had less than 30% depletion of chloride. In series B the influence of relative humidity on the reaction uptake was quantified for NaCl, a mixture of NaCl + $MgCl_2$ ($X_{Mg/Na} = 0.114$) and actual sea salt particles, all having $\bar{D}_p \sim 0.9$ μm

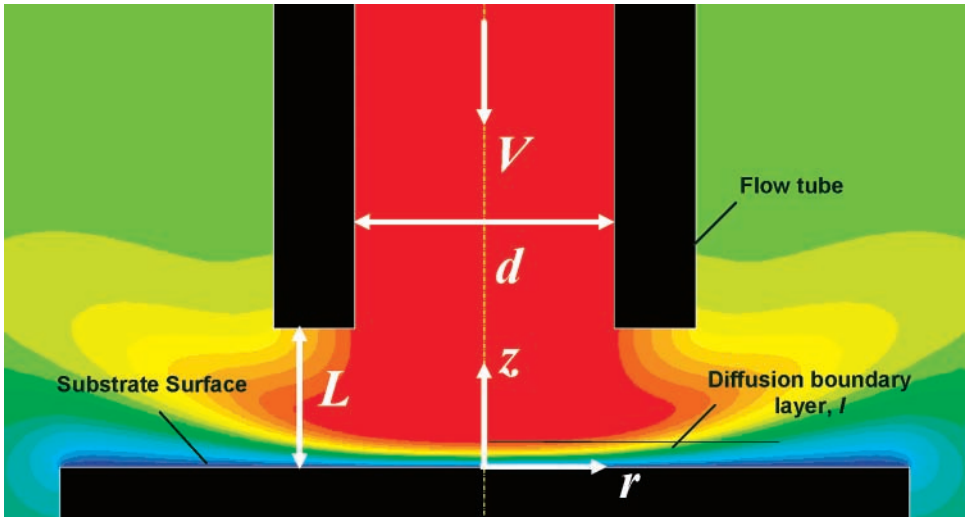

Figure 5. False-color contours of HNO_3 mass fraction computed with CFD modeling ($L = 0.4$ cm, $d = 0.8$ cm, $V = 2$ L/min, and $[HNO_3]_\infty = 1$ ppm). Red corresponds to the highest value, and dark blue, to the lowest.

(dry size). Tests in series B were performed under extremely small particle loading ($N_s < 5 \times 10^4$ cm^{-2}) to ensure that the measured uptake coefficient is that of the single-particle rate constant. Series C experiments measured the uptake coefficient as a function particle size (dry diameter, $\bar{D}_p = 0.54-1.7$ μm; wet diameter of deliquesced particles, $\bar{D}_d = 1.1-3.4$ μm) under RH = 80%. For series A and C experiments the influence of particle loading was eliminated by fitting the kinetic data as a function of particle surface density N_s using a diffusion-kinetic analysis, as will be discussed later.

Computational Fluid Dynamics

For particles larger than the mean free path of the gas, a key process in the uptake of nitric acid is its diffusion from the gas phase to the particle surface. Performing an accurate kinetic-diffusive analysis for the interpretation of experimental data requires that all particles experience the same or nearly the same (within a few percent) diffusive flux. The reactor implements a two-dimensional, axisymmetric reacting gas jet impingement onto NaCl particles deposited on a TEM substrate. The flow is similar to the well-studied Heimenz flow[90] but differs on two important aspects: diffusion is present and the jet inside the tube has a parabolic velocity profile arising from flowing through an upstream pipe. An analytical solution for this type of fluid motion, stagnation flow, exists only for a few special cases,[90,91] with this case not being one of them. Thus, we calculated the flow and HNO_3 diffusive flux numerically with FLUENT 6.2.[92] A computational domain of the reactor was created in FLUENT's pre-processor GAMBIT. Thin boundary layer cells (40 μm thick) were defined above the grid holder surface to capture the diffusion boundary layer. The model was then imported into FLUENT to numerically solve the mass, momentum, energy, and species conservation equations for incompressible, laminar flow. Boundary conditions were chosen such that the flow exiting the flow tube has a fully developed parabolic velocity profile, and the HNO_3 concentration immediately above the sample holder surface is zero. These conditions represent the "worst-case" scenario in terms of flow nonuniformity, as the entire sample holder surface acts as a complete sink to gaseous HNO_3.

Parametric studies were performed by varying three key reactor parameters shown in Figure 5: volumetric flow rate ($V = 0.25-4$ L/min), inlet tube diameter ($d = 0.4$ and 0.8 cm), and tube offset distance (L, with $L/d = {}^1/_4$ and ${}^1/_2$). The mass diffusivity of HNO_3 in N_2 was calculated from the Lennard-Jones potential parameters[92,93] of collision diameter $\sigma_{HNO_3-N_2} = (\sigma_{HNO_3} + \sigma_{N_2})/2$ and well depth $\epsilon_{HNO_3-N_2} = (\epsilon_{HNO_3}\epsilon_{N_2})^{1/2}$. For N_2, σ was taken to be 3.8 Å and $\epsilon/k_b = 71.4$ K,[94] where k_b is the Boltzmann constant. For HNO_3 the potential parameters were estimated from the critical properties[95] (critical volume $V_c = 145.0$ cm^3/mol and critical temperature $T_c = 520$ K) using empirical equations taken from Poling et al.[96] $\epsilon/k_b = T_c/1.2593$ and σ (Å) $= 0.809V_c^{1/3}$, where V_c and T_c are in the units of cm^3/mol and K, respectively. The diffusivity estimated in this manner is $D_{HNO_3-N_2} = 0.118$ cm^2/s at 300 K, which is in reasonable agreement with the value of 0.135 cm^2/s estimated by Abbatt and Waschewsky.[45]

Results and Discussion

CFD Simulations and Reactor Design. Typical spatial variations of HNO_3 concentration are shown in Figure 5. Along the centerline HNO_3 maintains its free stream concentration until a distance to the surface approximately 5% of the tube diameter, at which the diffusion boundary layer starts. Because the surface is assumed to be a complete sink for gaseous HNO_3, its concentration drops sharply toward the surface until it reaches a value of zero there. Comparison of the results shown in Figure 5 to a similar display for the radial velocity component (not shown) reveals very similar contours, indicating that flow convection plays a large part in transport of HNO_3 to the diffusion boundary layer, as anticipated.

Under the condition that the heterogeneous reaction is controlled by diffusion, the reaction rate is essentially determined by the boundary layer thickness (l). It is seen that the variation of this thickness is small near the tube centerline but increases notably toward the edge of the tube. For the parameter conditions chosen for the reactor ($d = 0.8$ cm, $L/d = {}^1/_4$, and $V = 2$ L/min), the boundary layer thickness is identical within a radius of $r = 0.25$ cm from the centerline and its thickness is no larger than ~0.05 cm, as seen in Figure 6. Even though this value is obtained for $[HNO_3]_\infty = 40$ ppm, similar results were obtained for 2, 20, and 200 ppm in terms of the HNO_3 concentration variation and the boundary layer thickness. Computations for free stream HNO_3 concentrations on the order of those in the experiment (a few ppb) could not be accurately resolved with FLUENT because of the large precision needed; thus, parts-per-million levels were used in modeling. Particles deposited on TEM grids placed within this radius of the

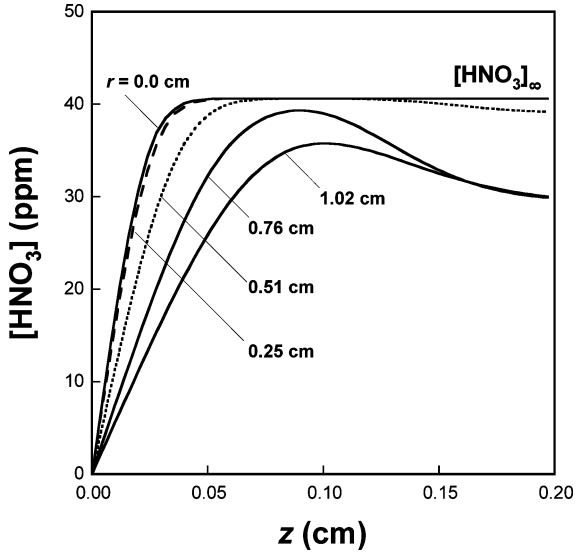

Figure 6. Axial variation of HNO_3 concentration normal to the substrate surface for several radial distances, computed for $d = 0.8$ cm, $L/d = 1/4$, $V = 2$ L/min, and $[HNO_3]_\infty = 40$ ppm in the free stream. The surface of the TEM grid holder corresponds to $z = 0$ cm, and the exit of the flow tube is at $z = 0.32$ cm.

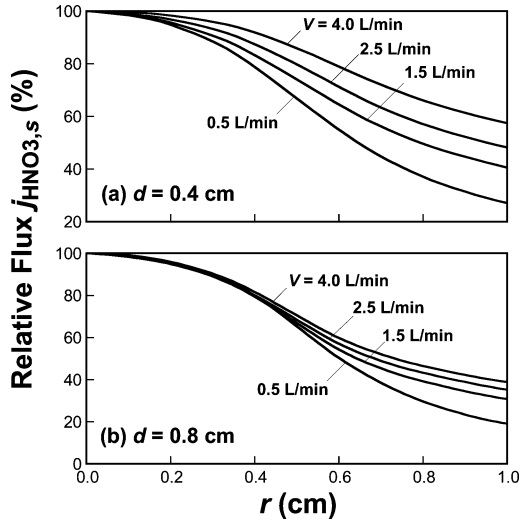

Figure 7. HNO_3 flux relative to that of the centerline ($r = 0$) immediately above the substrate surface, computed for $L/d = 1/4$, $[HNO_3]_\infty = 40$ ppm, and (a) $d = 0.4$ cm and (b) $d = 0.8$ cm.

centerline ($r = 0.25$ cm) are exposed to a nearly identical HNO_3 flux. Outside of this radius the diffusion flux of HNO_3 drops because of radial diffusion and momentum entrainment, leading to an increase in l.

The uniformity of the boundary layer in the radial direction with respect to reactor parameters may be further examined by plotting the diffusion flux $j_{HNO_3,s}$,

$$j_{HNO_3,s} = -D_{HNO_3-N_2} \left.\frac{d[HNO_3]}{dz}\right|_{surface} \quad (3)$$

Figure 7 shows the variation of $j_{HNO_3,s}$ normalized by its maximum value as a function of r and V. Comparing results obtained with the two different flow tube diameters, the radial variation of the diffusion flux is smaller for the larger tube ($d = 0.8$ cm) than that for the smaller tube ($d = 0.4$ cm). Also, the diffusion flux is less sensitive to flow rate variations for the larger tube. A similar effect is observed by decreasing the tube offset distance (L/d).

These computational results led us to choose $V = 2$ L/min, $d = 0.8$ cm and $L = 0.2$ cm ($L/d = 1/4$) for the experimental reactor. Under these conditions the HNO_3 flux within one TEM grid radius (~0.15 cm) is uniform to within 2%, even under the worst case scenario of the entire sample holder surface acting as an HNO_3 sink. The computational results also suggest that, under the current reactor design, multiple grids may be placed near the centerline of the jet especially with a finite rate of reaction.

An additional computational test was performed by assuming that only the grid surface acts as a sink to gaseous HNO_3, instead of the entire grid holder surface. Figure 8 shows the high degree of uniformity for $[HNO_3]$ above the grid surface. The changes toward the edge of the disc are caused by discontinuity in the surface boundary condition (i.e., going from the free stream value outside the grid to zero at the grid surface). The distance over which this occurs is negligible. As shown in Figure 9, the profile of the HNO_3 concentration is identical within a radius of 0.13 cm. The concentration profile varies markedly only within 0.1 mm from the grid perimeter, where the particle samples are excluded from the experimental analysis. Note that the nonzero value computed for $r = 0.15$ cm arises from the jump condition imposed in the CFD analysis to avoid discontinuity. The point intended to be made is clearly shown: the diffusive flux is constant over a majority of the grid surface.

Apparent Pseudo-First-Order and Intrinsic Second-Order Rate Constants. As seen in eq 2, CCSEM/EDX analysis measures the overall Cl^- loss from dry residues of the NaCl particles, which can be expressed as follows:

$$-\frac{d[Cl^-]_d}{dt} = k_I[Cl^-]_d \quad (4)$$

where $[Cl^-]_d$ is the molar concentration of Cl^- in deliquesced NaCl particles. If the apparent, pseudo-first-order rate constant k_I is a constant during reaction, its value may be estimated from

$$k_I = -\frac{1}{t}\ln\left(\frac{[Cl^-]_{d,t}}{[Cl^-]_{d,t=0}}\right) = -\frac{1}{t}\ln\left(\frac{[Cl/Na]_t^{EDX}}{[Cl/Na]_{t=0}^{EDX}}\right) \quad (5)$$

Table 2 lists the $[Cl/Na]_{d,t}^{EDX}/[Cl/Na]_{d,t=0}^{EDX}$ and k_I values experimentally determined for series A experiments with dry-particle diameter $\bar{D}_p \sim 0.8$ μm under the relative humidity of RH = 80%. In this series of experiments the HNO_3 concentration in the free stream was varied from 2 to 22 ppb. The data given in the table allow us to determine the second-order rate constant, k_{II}, which is related to k_I by

$$k_I = k_{II}[HNO_3]_s \quad (6)$$

Because of diffusive competition for HNO_3 among adjacent droplets, the HNO_3 concentration immediately above the droplet surface $[HNO_3]_s$ is expected to be smaller than the free stream value. Thus, k_I depends on both k_{II} and the gas-phase diffusion rate to the substrate surface, which is dependent on the particle surface density N_s. It should be noted that the second-order rate constant does not always measure the chemical reaction rate, because the reaction rate of a single particle may still be diffusion-controlled.

A previous diffusion-kinetic analysis[86] used a one-dimensional model of coupled gas-surface reaction and gas diffusion through

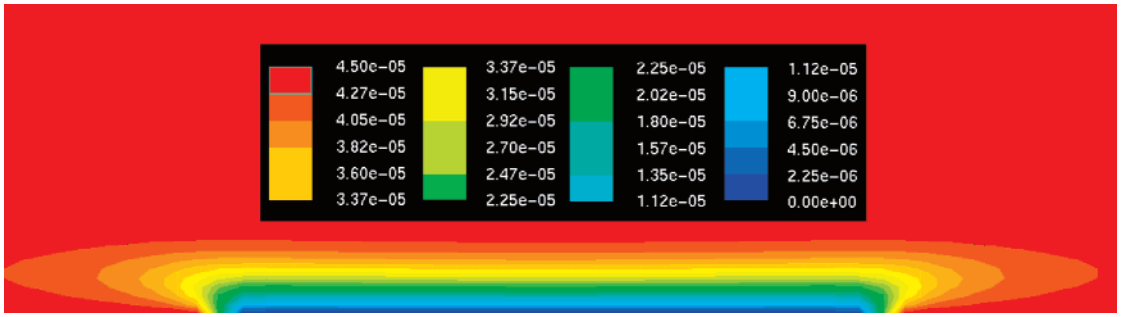

Figure 8. Mass fraction contours of [HNO_3] directly above the grid (diameter = 0.3 cm). Boundary conditions are $[HNO_3]_\infty = 20$ ppm and [HNO_3] = 0 on the grid surface. The computation used $L = 0.2$ cm, $d = 0.8$ cm, and $V = 2$ L/min.

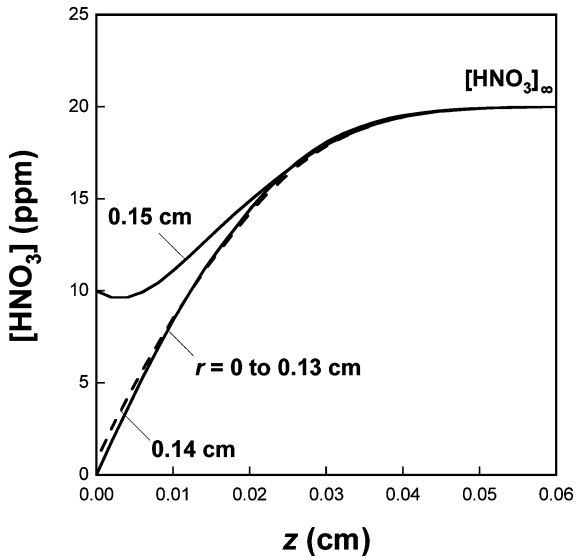

Figure 9. Axial variation of [HNO_3] at several different radii for the computational case described in Figure 8. The profiles at locations within $r = 0$ to 0.13 cm are exactly the same.

a stagnant gas film above the substrate surface, and showed that k_I may be related to N_s by

$$\frac{[HNO_3]_\infty}{k_I} = \left[\frac{(1+\delta k_s)}{k_{II}} + V_d[Cl^-]_{d,0}\delta e^{-k_I t}\cdot N_s\right] \qquad (7)$$

In the above equation k_s is the rate constant of HNO_3 reaction with the substrate surface, δ is a parameter and equal to $l/D_{HNO_3-N_2}$ and V_d is the droplet volume. Equation 7 shows that $[HNO_3]_\infty/k_I$ varies linearly with N_s: the intercept is related to the second-order rate constant in the limit of low surface density $N_s \rightarrow 0$ and the slope is $V_d[Cl^-]_{d,0}\delta e^{-k_I t}$. Figure 10 shows the $[HNO_3]_\infty/k_I$ data of Table 2 plotted as a function of particle loading. Despite the fact that b depends on $e^{-k_I t}$, δ and V_d, all of which vary with time, the variation of the product $V_d\delta e^{-k_I t}$ has been shown to be insignificant.[86]

As expected from eq 7 and confirmed from the data shown in Figure 10, the pseudo first-order rate constant depends on the particle loading N_s, but whether the observed rate constant is time invariant remains a question. We analyzed the $[HNO_3]_\infty/k_I$ values taken at several particle loadings but over a range of reaction times ($8 < t < 300$ min). The analysis shows no discernible, systematic variation of $[HNO_3]_\infty/k_I$ as a function of time, as shown in Figure S1 of the Supporting Information. In addition, the fact that the $[HNO_3]_\infty/k_I$ values shown in Figure 10 overlap reasonably well among the three experimental series confirms the pseudo-first-order reaction conditions of our experiments and that the first-order rate constant is indeed time invariant over the range of reaction time studied.

The solid line of Figure 10 represents the fit to data using eq 7. The fitting includes only data of Table 2 (solid symbols), all of which were observed for $N_s > 4 \times 10^4$ cm^{-2}. The data clearly cluster around the fitted line with a degree of scatter consistent with the uncertainties of the data points. We also included in the figure an auxiliary set of data obtained for $\bar{D}_p = 0.77$ μm under the relative humidity of RH = 80% but with quite small N_s values (Table 3). Again, these data values are consistent with the fit. The intercept is found to be 1.8×10^{14} cm^{-3} s. Assuming $\delta k_s \ll 1$ for the experiment yielded $k_{II} = 5.7 \times 10^{-15}$ cm^3 molecule^{-1} s^{-1} with an uncertainty of a factor of ~3, as shown by the dashed lines of Figure 10.

The surface reaction rate constant k_s is the product of the sticking probability and the wall collision rate constant. Though some loss of HNO_3 to the substrate might occur, it cannot be very large, as a dependence of chloride loss on N_s would not have been observed. The sticking probability of HNO_3 on carbon substrate has not been determined. For the assumption $\delta k_s \ll 1$ to be valid, this probability must be smaller than 10^{-4}, which is quite reasonable considering that the HNO_3 vapor concentration employed in the current experiment is substantially below its saturation pressure at 300 K ($P_{sat} = 6 \times 10^{-5}$ atm).

Equations 4−7 assume formal stoichiometry of reaction 1: the uptake of 1 molecule of HNO_3 (or the formation of nitrate in particle) corresponds to the loss of 1 chloride ion. This assumption was verified from changes observed for both N-to-Na and O-to-Na atomic ratios of reacted particles. The pseudo-first-order rate constants, determined from $[N/Na]_t^{EDX}$ and $[O/Na]_t^{EDX}$, are compared to those determined from $[Cl/Na]_t^{EDX}$, as shown in Figure S2 of the Supporting Information. The close match of the three data sets indicates that indeed the reaction stoichiometry is conserved over the experimental conditions of this study. In principle, any of the three data sets could be used for k_I determination, but the quantitative detection of low-Z elements, such as N and O, is typically less accurate than Cl because of a number of inherent constrains of the CCEM/EDX particle analysis.[85]

Experimental Net Uptake Coefficient. The experimental net uptake coefficient γ_{net} is customarily calculated by

$$\gamma_{net} = \frac{4k_I^*[Cl^-]_{d,0}}{\bar{c}_{HNO_3}[HNO_3]_\infty}\frac{V_d}{S_d} = \frac{2k_{II}[Cl^-]_{d,0}\bar{D}_d}{3\bar{c}_{HNO_3}} \qquad (8)$$

where k_I^* is the apparent, pseudo-first-order rate constant in the limit of $N_s \rightarrow 0$, V_d/S_d is the droplet volume-to-surface area ratio, $\bar{c}_{HNO_3} = 3.18 \times 10^4$ cm/s is the mean molecular speed of HNO_3, and $\bar{D}_d$ is the deliquesced droplet diameter. Equation 8 would be exact if the heterogeneous reaction occurs around the

TABLE 2: Summary of Experimental Conditions (Series a) and Pseudo-First-Order Rate Constants[a]

$10^{-4}N_s$ (cm^{-2})	time (min)	$[Cl/Na]_t^{EDX}$	$[Cl/Na]_{t=0}^{EDX}$	10^6k_I (s^{-1})	$10^{-4}N_s$ (cm^{-2})	time (min)	$[Cl/Na]_t^{EDX}$	$[Cl/Na]_{t=0}^{EDX}$	10^6k_I (s^{-1})
A1: $[HNO_3]_\infty = 2.0 \pm 0.0$ ppb, $\bar{D}_p = 0.76 \pm 0.04$ μm									
4 ± 0	35	0.73 ± 0.17	1.11 ± 0.05	197 (× 1.7/÷2.1)	74 ± 13	150	0.71 ± 0.12	1.11 ± 0.05	50 (× 1.4/÷1.6)
4 ± 2	35	0.52 ± 0.16	1.11 ± 0.05	361 (× 1.5/÷1.6)	81 ± 12	150	0.73 ± 0.11	1.11 ± 0.05	46 (× 1.4/÷1.5)
5 ± 2	30	0.75 ± 0.18	1.11 ± 0.05	215 (× 1.7/÷2.3)	85 ± 27	180	0.73 ± 0.19	1.12 ± 0.05	39 (× 1.7/÷2.3)
6 ± 2	30	0.82 ± 0.15	1.11 ± 0.05	166 (× 1.7/÷2.4)	105 ± 23	180	0.67 ± 0.12	1.12 ± 0.05	48 (× 1.4/÷1.5)
6 ± 2	30	0.75 ± 0.20	1.11 ± 0.05	218 (× 1.8/÷2.6)	121 ± 24	120	0.93 ± 0.07	1.11 ± 0.05	24 (× 1.5/÷1.9)
8 ± 3	30	0.85 ± 0.11	1.11 ± 0.05	148 (× 1.6/÷1.9)	219 ± 52	300	0.95 ± 0.10	1.12 ± 0.05	9 (× 1.8/÷3.1)
12 ± 3	30	0.87 ± 0.16	1.11 ± 0.05	135 (× 1.9/÷3.5)	253 ± 48	300	0.97 ± 0.08	1.11 ± 0.05	7 (× 1.7/÷2.9)
13 ± 2	30	0.92 ± 0.15	1.11 ± 0.05	102 (× 2.0/÷6.9)	658 ± 150	720	0.96 ± 0.07	1.11 ± 0.05	3 (× 1.6/÷2.3)
26 ± 8	25	0.93 ± 0.14	1.11 ± 0.05	115 (× 2.0/÷6.4)	765 ± 170	720	0.99 ± 0.09	1.11 ± 0.05	3 (× 1.9/÷6.0)
31 ± 8	25	0.95 ± 0.13	1.11 ± 0.05	102 (× 2.0/÷7.9)					
A2: $[HNO_3]_\infty = 6.8 \pm 0.7$ ppb, $\bar{D}_p = 0.81 \pm 0.08$ μm									
9 ± 3	10	0.96 ± 0.12	1.12 ± 0.05	250 (× 2.0/÷6.4)	78 ± 7	60	0.91 ± 0.07	1.10 ± 0.05	52 (× 1.5/÷1.8)
11 ± 3	10	0.99 ± 0.10	1.12 ± 0.05	206 (× 2.0/÷7.5)	86 ± 8	45	0.98 ± 0.07	1.11 ± 0.06	45 (× 1.8/÷3.4)
12 ± 3	10	0.95 ± 0.12	1.12 ± 0.05	266 (× 1.9/÷4.9)	89 ± 7	45	0.95 ± 0.11	1.11 ± 0.06	57 (× 1.9/÷4.9)
18 ± 9	20	0.83 ± 0.18	1.10 ± 0.05	225 (× 1.6/÷2.1)	98 ± 18	60	0.97 ± 0.06	1.10 ± 0.05	34 (× 1.6/÷2.5)
22 ± 10	20	0.86 ± 0.15	1.10 ± 0.05	206 (× 1.8/÷3.1)	105 ± 22	60	0.90 ± 0.12	1.11 ± 0.06	57 (× 1.8/÷2.9)
24 ± 9	20	0.84 ± 0.12	1.10 ± 0.05	223 (× 1.6/÷2.1)	107 ± 13	60	0.94 ± 0.07	1.10 ± 0.05	43 (× 1.6/÷2.2)
26 ± 7	20	0.89 ± 0.12	1.10 ± 0.05	174 (× 1.7/÷2.7)	116 ± 35	60	0.97 ± 0.10	1.11 ± 0.06	37 (× 1.9/÷6.4)
39 ± 15	20	0.87 ± 0.17	1.10 ± 0.05	191 (× 2.0/÷4.7)	319 ± 28	200	0.97 ± 0.05	1.10 ± 0.06	10 (× 1.6/÷2.5)
53 ± 13	20	0.99 ± 0.07	1.11 ± 0.05	93 (× 1.8/÷3.7)	348 ± 39	200	0.98 ± 0.05	1.10 ± 0.05	9 (× 1.6/÷2.4)
54 ± 11	20	0.97 ± 0.08	1.11 ± 0.05	111 (× 1.8/÷3.2)					
A3: $[HNO_3]_\infty = 22 \pm 2$ ppb, $\bar{D}_p = 0.85 \pm 0.09$ μm									
33 ± 7	10	0.85 ± 0.20	1.10 ± 0.05	431 (× 2.0/÷5.7)	105 ± 21	12	0.90 ± 0.08	1.11 ± 0.05	287 (× 1.5/÷1.8)
36 ± 23	10	0.81 ± 0.13	1.10 ± 0.05	498 (× 1.6/÷2.1)	165 ± 30	20	0.84 ± 0.09	1.14 ± 0.05	252 (× 1.4/÷1.6)
41 ± 29	10	0.91 ± 0.12	1.10 ± 0.05	315 (× 1.8/÷3.3)	180 ± 39	25	0.82 ± 0.12	1.13 ± 0.05	211 (× 1.5/÷1.8)
44 ± 8	10	0.90 ± 0.17	1.10 ± 0.05	329 (× 2.1/÷9.6)	199 ± 38	25	0.73 ± 0.31	1.13 ± 0.05	302 (× 2.3/÷5.2)
45 ± 10	10	0.75 ± 0.12	1.10 ± 0.05	632 (× 1.5/÷1.7)	204 ± 25	25	0.86 ± 0.11	1.13 ± 0.05	180 (× 1.5/÷1.9)
53 ± 23	40	0.17 ± 0.07	1.09 ± 0.06	772 (× 1.3/÷1.2)	243 ± 68	20	0.85 ± 0.09	1.10 ± 0.05	213 (× 1.5/÷1.8)
55 ± 18	10	0.85 ± 0.18	1.10 ± 0.06	418 (× 2.0/÷4.6)	254 ± 39	20	0.93 ± 0.15	1.12 ± 0.06	153 (× 2.0/÷7.0)
71 ± 31	10	0.70 ± 0.18	1.13 ± 0.05	801 (× 1.6/÷1.9)	285 ± 24	25	0.87 ± 0.14	1.13 ± 0.05	171 (× 1.7/÷2.5)
81 ± 28	15	0.70 ± 0.15	1.10 ± 0.05	503 (× 1.6/÷1.8)	286 ± 33	20	0.84 ± 0.08	1.14 ± 0.05	253 (× 1.4/÷1.5)
104 ± 23	25	0.59 ± 0.14	1.13 ± 0.05	429 (× 1.4/÷1.5)	326 ± 59	20	0.94 ± 0.08	1.11 ± 0.05	136 (× 1.6/÷2.2)

[a] All of the experiments were conducted at RH = 80%. Uncertainty values represent one-standard deviation. k_I is the apparent, pseudo-first-order rate constant of chloride loss, determined from eq 5, and the uncertainty factors in parentheses correspond to ± one standard deviation in $[Cl/Na]_t^{EDX}$ and $[Cl/Na]_{t=0}^{EDX}$.

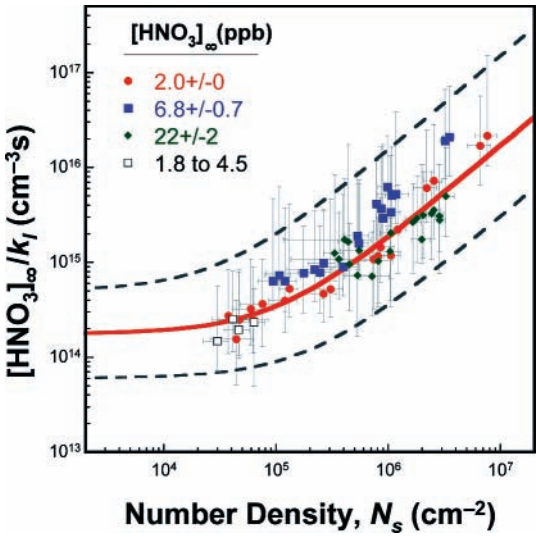

Figure 10. Experimental values of $[HNO_3]_\infty/k_I$, measured for ~0.8 μm NaCl particles and RH = 80%, as a function of particle number density N_s on the substrate surface. Key: symbols, experimental data; line, fit to data. The error bar on each data point represents one standard deviation for $[Cl]_{d,t}/[Cl]_{d,t=0}$. Dashed lines represent the uncertainties of the fit.

entire sphere of the droplet. As will be shown later, the reactive uptake observed in the present study is largely controlled by diffusion of gaseous HNO_3 onto individual droplets even in the limit of $N_s \rightarrow 0$. The substrate-based experiment inherently limits the diffusion flux of the gaseous reactant over a hemisphere rather than the entire sphere. Thus, a simple correction has to be made to account for this effect, which effectively increase the uptake coefficient by a factor of 2, i.e.,

$$\gamma_{net} = \frac{4k_{II}[Cl^-]_{d,0}\bar{D}_d}{3\bar{c}_{HNO_3}} \quad (9)$$

The above equation was used in all subsequent analysis to obtain the uptake coefficient.

The droplet diameter $\bar{D}_d$ may be calculated from the known dry particle diameter and thermodynamic properties and hygroscopic growth data of NaCl particles.[97] Under 80% RH, $[Cl^-]_{d,0} = 5$ M and the ratio of droplet to dry particle diameters $\bar{D}_d/\bar{D}_p = 2$, i.e., 0.8 μm dry NaCl particles become 1.6 μm droplets when deliquesced. Using this $\bar{D}_d$ value and the k_{II} value discussed earlier, we obtain $\gamma_{net} \geq 0.11$ (×2.9/÷2.8) for RH = 80%. In spite of the size effect on reactive uptake (to be discussed later), this value is about a factor of 2 larger than initial net uptake coefficient reported by Saul et al.[53] ($\gamma_{net,0} = 0.05$) for much smaller droplets ($\bar{D}_d = 0.1$ μm) under the same humidity. In addition, the current γ_{net} value is a factor of 2 smaller than that Abbatt and Waschewsky[45] obtained for 3 μm deliquesced NaCl droplets under 75% relative humidity. The current uptake coefficient is similar to those reported for HNO_3 uptake onto water droplets (γ_{net} ranging from 0.03 to 0.11) from droplet train and single droplet studies.[98−101] Similar observations were reported for heterogeneous N_2O_5 uptake onto sea

TABLE 3: Summary of Experimental Conditions (Series B) and Pseudo-First-Order Rate Constants[a]

$[HNO_3]_\infty$ (ppb)	$10^{-4}N_s$ (cm^{-2})	time (min)	$[Cl/Na]_t^{EDX}$	$[Cl/Na]_{t=0}^{EDX}$	$10^5 k_I$ (s^{-1})
			Series B1: NaCl		
			RH = 80%; $\bar{D}_p = 0.77 \pm 0.05$ μm		
4.0	6.3 ± 1.6	30	0.47 ± 0.09	1.08 ± 0.05	4.6 (×1.3/÷1.3)
4.5	4.1 ± 1.0	20	0.60 ± 0.22	1.07 ± 0.07	4.8 (×1.8/÷2.3)
3.0	4.6 ± 1.2	20	0.64 ± 0.25	1.06 ± 0.05	4.2 (×2.0/÷3.0)
1.8	3.6 ± 0.9	20	0.82 ± 0.22	1.06 ± 0.05	2.2 (×2.2/*b*)
2.0	3.0 ± 0.7	20	0.70 ± 0.22	1.07 ± 0.05	3.5 (×1.9/÷2.9)
			RH = 70%; $\bar{D}_p = 0.80 \pm 0.05$ μm		
2.0	3.1 ± 0.8	25	0.77 ± 0.29	1.07 ± 0.05	2.2 (×2.5/÷*b*)
2.0	7.9 ± 2.0	25	0.81 ± 0.17	1.07 ± 0.05	1.8 (×1.9/÷3.4)
2.5	4.5 ± 1.1	15	0.76 ± 0.19	1.07 ± 0.05	3.8 (×1.8/÷2.9)
2.4	2.4 ± 0.6	15	0.80 ± 0.17	1.07 ± 0.05	3.3 (×1.8/÷3.1)
2.2	4.5 ± 1.1	15	0.86 ± 0.18	1.06 ± 0.05	2.3 (×2.2/÷*b*)
			RH = 60%; $\bar{D}_p = 0.84 \pm 0.05$ μm		
3.5	2.1 ± 0.5	15	0.65 ± 0.18	1.02 ± 0.07	4.9 (×1.8/÷2.3)
3.0	4.6 ± 1.2	15	0.71 ± 0.14	1.03 ± 0.07	4.1 (×1.6/÷2.1)
2.8	2.3 ± 0.6	15	0.75 ± 0.16	1.02 ± 0.07	3.4 (×1.8/÷2.9)
2.6	4.5 ± 1.1	10	0.84 ± 0.13	1.03 ± 0.06	3.4 (×1.9/÷4.2)
2.6	3.0 ± 0.7	10	0.89 ± 0.12	1.03 ± 0.06	2.4 (×2.1/÷*b*)
			RH = 50%; $\bar{D}_p = 0.82 \pm 0.05$ μm		
2.0	2.1 ± 0.5	8	0.95]±0.18	1.04 ± 0.07	1.8 (×3.6/÷*b*)
2.8	3.6 ± 0.9	10	0.86 ± 0.17	1.04 ± 0.07	3.1 (×2.3/÷*b*)
2.8	3.2 ± 0.8	10	0.88 ± 0.20	1.04 ± 0.05	2.8 (×2.6/÷*b*)
3.5	2.7 ± 0.7	10	0.75 ± 0.18	1.04 ± 0.05	5.4 (×1.9/÷3.1)
3.5	1.7 ± 0.4	10	0.70 ± 0.20	1.04 ± 0.05	6.6 (×1.9/÷2.9)
			RH = 40%; $\bar{D}_p = 0.76 \pm 0.03$ μm		
3.6	2.1 ± 0.5	20	0.84 ± 0.12	1.04 ± 0.07	1.7 (×1.8/÷3.5)
3.7	4.9 ± 1.2	20	0.83 ± 0.14	1.04 ± 0.07	1.8 (×1.9/÷4.1)
3.5	3.7 ± 0.9	20	0.93 ± 0.11	1.04 ± 0.07	0.9 (×2.4/÷*b*)
3.6	4.2 ± 1.1	20	0.88 ± 0.16	1.04 ± 0.07	1.3 (×2.3/÷*b*)
3.5	2.9 ± 0.7	25	0.86 ± 0.14	1.04 ± 0.07	1.2 (×2.1/÷8.2)
			RH = 30%; $\bar{D}_p = 0.78 \pm 0.03$ μm		
4.1	2.7 ± 0.7	30	0.93 ± 0.06	1.04 ± 0.07	0.6 (×1.9/÷5.4)
4.1	3.2 ± 0.8	30	0.88 ± 0.08	1.04 ± 0.07	0.9 (×1.7/÷2.8)
3.9	3.1 ± 0.8	36	0.87 ± 0.15	1.04 ± 0.07	0.8 (×2.2/÷*b*)
3.9	3.2 ± 0.8	30	0.94 ± 0.07	1.04 ± 0.07	0.5 (×2.1/÷*b*)
3.9	4.1 ± 1.0	30	0.92 ± 0.07	1.04 ± 0.07	0.7 (×1.9/÷6.0)
			RH = 20%; $\bar{D}_p = 0.75 \pm 0.04$ μm		
4.5	3.6 ± 0.9	60	0.92 ± 0.18	1.04 ± 0.07	0.3 (×3.1/÷*b*)
4.5	3.8 ± 1.0	60	0.84 ± 0.21	1.04 ± 0.07	0.6 (×2.4/÷*b*)
4.4	3.0 ± 0.7	60	0.85 ± 0.26	1.04 ± 0.07	0.6 (×2.9/÷*b*)
4.4	4.7 ± 1.2	60	0.95 ± 0.08	1.04 ± 0.07	0.2 (×2.4/÷*b*)
4.4	2.0 ± 0.5	60	0.95 ± 0.09	1.04 ± 0.07	0.2 (×2.4/÷*b*)
			Series B2: $NaCl/MgCl_2$ ($X_{Mg/Na} = 0.114$)		
			RH = 80%; $\bar{D}_p = 0.87 \pm 0.02$ μm		
2.2	2.4 ± 0.6	10	0.95 ± 0.14	1.10 ± 0.07	2.4 (×2.2/÷*b*)
2.0	5.0 ± 1.3	10	0.97 ± 0.17	1.10 ± 0.09	2.0 (×2.8/÷*b*)
2.0	4.6 ± 1.2	10	1.02 ± 0.12	1.10 ± 0.09	1.1 (×3.4/÷*b*)
2.0	3.2 ± 0.8	10	0.98 ± 0.12	1.10 ± 0.09	1.8 (×2.4/÷*b*)
			RH = 70%; $\bar{D}_p = 0.94 \pm 0.03$ μm		
1.9	6.0 ± 1.5	10	0.97 ± 0.29	1.10 ± 0.08	2.1 (×4.0/÷*b*)
1.9	3.9 ± 1.0	10	0.98 ± 0.10	1.10 ± 0.08	1.8 (×2.2/÷*b*)
1.8	3.5 ± 0.9	10	1.00 ± 0.09	1.10 ± 0.08	1.5 (×2.4/÷*b*)
2.0	5.7 ± 1.4	10	0.95 ± 0.13	1.10 ± 0.08	2.3 (×2.2/÷*b*)
			RH = 60%; $\bar{D}_p = 0.89 \pm 0.03$ μm		
2.4	3.2 ± 0.8	15	0.78 ± 0.19	1.10 ± 0.07	3.8 (×1.9/÷2.9)
2.5	5.2 ± 1.3	15	0.79 ± 0.24	1.10 ± 0.07	3.6 (×2.2/÷6.5)
2.2	11.0 ± 2.8	10	0.95 ± 0.20	1.10 ± 0.07	2.5 (×2.7/÷*b*)
2.3	10.7 ± 2.7	10	0.97 ± 0.15	1.10 ± 0.07	2.0 (×2.5/÷*b*)
			RH = 50%; $\bar{D}_p = 0.89 \pm 0.02$ μm		
2.2	5.7 ± 1.4	8	1.00 ± 0.08	1.10 ± 0.07	1.9 (×2.2/÷*b*)
2.1	9.8 ± 2.4	5	1.01 ± 0.10	1.10 ± 0.07	2.7 (×2.6/÷*b*)
2.1	6.3 ± 1.6	5	1.01 ± 0.10	1.10 ± 0.07	2.8 (×2.5/÷*b*)
			RH = 40%; $\bar{D}_p = 0.87 \pm 0.04$ μm		
5.6	3.3 ± 0.8	15	0.92 ± 0.09	1.10 ± 0.07	1.9 (×1.7/÷2.8)
5.2	2.3 ± 0.6	10	0.96 ± 0.06	1.10 ± 0.07	2.2 (×1.7/÷2.9)
5.1	5.7 ± 1.4	10	0.91 ± 0.12	1.10 ± 0.07	3.1 (×1.9/÷4.1)
4.8	7.6 ± 1.9	10	0.94 ± 0.08	1.10 ± 0.07	2.5 (×1.8/÷3.1)

TABLE 3 (Continued)

$[HNO_3]_\infty$ (ppb)	$10^{-4}N_s$ (cm^{-2})	time (min)	$[Cl/Na]_t^{EDX}$	$[Cl/Na]_{t=0}^{EDX}$	$10^5 k_I$ (s^{-1})
		RH = 30%; $\bar{D}_p = 0.83 \pm 0.02$ μm			
6.0	4.2 ± 1.0	30	0.83 ± 0.29	1.10 ± 0.07	1.6 (×2.6/÷*b*)
6.5	2.3 ± 0.6	30	0.90 ± 0.11	1.10 ± 0.07	1.1 (×1.8/÷2.9)
6.0	3.3 ± 0.8	30	0.80 ± 0.20	1.10 ± 0.07	1.7 (×2.0/÷3.8)
6.0	3.7 ± 0.9	30	0.83 ± 0.21	1.10 ± 0.07	1.5 (×2.1/÷6.0)
		RH = 20%; $\bar{D}_p = 0.92 \pm 0.05$ μm			
4.8	7.4 ± 1.8	60	0.92 ± 0.08	1.10 ± 0.07	0.5 (×1.6/÷2.4)
5.0	3.3 ± 0.8	60	0.73 ± 0.22	1.10 ± 0.07	1.2 (×1.9/÷2.9)
4.6	3.5 ± 0.9	60	0.91 ± 0.13	1.10 ± 0.07	0.5 (×1.9/÷4.4)
4.4	8.3 ± 2.1	60	1.00 ± 0.12	1.10 ± 0.07	0.3 (×2.5/÷*b*)
		Series B3: Sea Salt			
		RH = 80%; $\bar{D}_p = 0.83 \pm 0.02$ μm			
3.0	3.0 ± 0.7	15	0.79 ± 0.16	0.99 ± 0.11	2.3 (×2.3/÷*b*)
3.0	2.0 ± 0.5	10	0.81 ± 0.26	1.01 ± 0.13	3.4 (×3.2/÷*b*)
2.4	2.3 ± 0.6	10	0.90 ± 0.16	1.01 ± 0.15	1.5 (×4.0/÷*b*)
2.1	2.8 ± 0.7	10	0.91 ± 0.26	1.02 ± 0.13	1.5 (×5.3/÷*b*)
		RH = 70%; $\bar{D}_p = 0.90 \pm 0.05$ μm			
3.0	6.0 ± 1.5	15	0.76 ± 0.23	1.02 ± 0.18	2.9 (×2.8/÷*b*)
3.1	3.6 ± 0.9	15	0.76 ± 0.25	1.01 ± 0.15	2.9 (×2.8/÷*b*)
2.8	3.2 ± 0.8	15	0.74 ± 0.25	1.01 ± 0.15	3.2 (×2.6/÷*b*)
		RH = 60%; $\bar{D}_p = 0.89 \pm 0.05$ μm			
2.0	3.2 ± 0.8	10	0.83 ± 0.23	1.01 ± 0.15	2.9 (×3.3/÷*b*)
2.0	4.6 ± 1.2	10	0.89 ± 0.18	1.01 ± 0.15	1.7 (×3.9/÷*b*)
1.9	1.1 ± 0.3	10	0.85 ± 0.24	1.01 ± 0.15	2.4 (×3.7/÷*b*)
2.0	3.9 ± 1.0	10	0.86 ± 0.10	1.01 ± 0.15	2.3 (×2.6/÷*b*)
		RH = 50%; $\bar{D}_p = 0.88 \pm 0.04$ μm			
2.3	7.7 ± 1.9	15	0.78 ± 0.17	1.01 ± 0.15	2.6 (×2.3/÷*b*)
2.4	5.7 ± 1.4	15	0.70 ± 0.16	1.01 ± 0.15	3.8 (×2.0/÷3.5)
2.3	3.9 ± 1.0	10	0.87 ± 0.26	1.01 ± 0.15	2.1 (×4.4/÷*b*)
		RH = 40%; $\bar{D}_p = 0.92 \pm 0.04$ μm			
3.5	3.3 ± 0.8	15	0.89 ± 0.38	1.01 ± 0.15	1.3 (×6.6/÷*b*)
4.5	4.0 ± 1.0	15	0.75 ± 0.33	1.01 ± 0.15	3.2 (×3.4/÷*b*)
3.5	5.7 ± 1.4	15	0.85 ± 0.33	1.01 ± 0.15	1.6 (×4.9/÷*b*)
3.0	6.9 ± 1.7	15	0.91 ± 0.23	1.01 ± 0.15	0.9 (×5.6/÷*b*)
		RH = 30%; $\bar{D}_p = 1.01 \pm 0.09$ μm			
6.5	4.8 ± 1.2	30	0.85 ± 0.25	1.20 ± 0.09	1.9 (×2.1/÷4.9)
5.5	6.4 ± 1.6	25	1.01 ± 0.13	1.19 ± 0.08	1.1 (×2.0/÷6.5)
5.0	5.4 ± 1.4	25	1.01 ± 0.11	1.13 ± 0.15	0.6 (×3.1/÷*b*)
5.0	6.1 ± 1.5	25	1.02 ± 0.12	1.19 ± 0.15	0.9 (×2.5/÷*b*)
		RH = 20%; $\bar{D}_p = 0.95 \pm 0.10$ μm			
4.0	2.5 ± 0.6	60	1.04 ± 0.08	1.16 ± 0.15	0.3 (×2.8/÷*b*)
4.0	4.5 ± 1.1	60	1.00 ± 0.14	1.14 ± 0.12	0.3 (×2.6/÷*b*)
4.0	2.7 ± 0.7	60	1.02 ± 0.15	1.19 ± 0.15	0.4 (×2.6/÷*b*)

[a] Uncertainty values represent one-standard deviation; k_I is the apparent, pseudo-first-order rate constant of chloride loss, determined from eq 5, and the uncertainty factors in parentheses correspond to ± one standard deviation in $[Cl/Na]_t^{EDX}$ and $[Cl/Na]_{t=0}^{EDX}$. [b] The lower limit cannot be determined because of the small extent of reaction; i.e., the lower uncertainty limit is given by zero extent of reaction.

salt and water droplets,[54,102,103] all of which are likely to stem from gas-phase diffusion being a rate-limiting step, as will be elaborated further in the size dependence section of this manuscript.

RH Dependence. Relative humidity varies widely in the atmosphere, ranging from a highly moist environment (RH > 80%) in the marine boundary layer to very arid condition in the upper troposphere. Thus, it is of particular interest to quantify the effects of relative humidity on the reactive uptake. In series B experiments the uptake coefficient was determined over the RH range of 20−80%. The conditions employed and kinetic data obtained for this series of experiments are listed in Table 3, which includes data for pure NaCl, the $NaCl/MgCl_2$ mixture, and real sea salt. The particle loadings were consistently small ($N_s < 10^5$ cm^{-2}) in comparison to series A experiments, thus ensuring all measurements to be in the limit of small particle loading, as demonstrated in Figure 10.

According to eq 9 the size of deliquesced or effloresced particles is required for uptake coefficient calculation. Dry particle size $\bar{D}_p$ can be obtained from CCSEM data. Because the growth factor of NaCl and sea salt particles relative to their dry forms can be calculated on the basis of Tang's results,[97] we were also able to determine droplet diameter $\bar{D}_d$ of deliquesced particles at a given RH. Also, RH-dependent chloride concentration in NaCl and mixture of $NaCl/MgCl_2$ has been reported recently.[53] The growth factor of $NaCl/MgCl_2$ and $[Cl^-]$ in the sea salt are not yet available and had to be estimated from the growth factor of the sea salt and the $[Cl^-]$ in the mixture of $NaCl/MgCl_2$, respectively. We do not expect that the results would be considerably affected by these assumptions.

Figure 11 shows uptake coefficients measured over a broad range of RH for NaCl particles with $\bar{D}_p \sim 0.9$ μm. The overall trend and values of HNO_3 uptake are in good agreement with data published previously, although the agreement may be

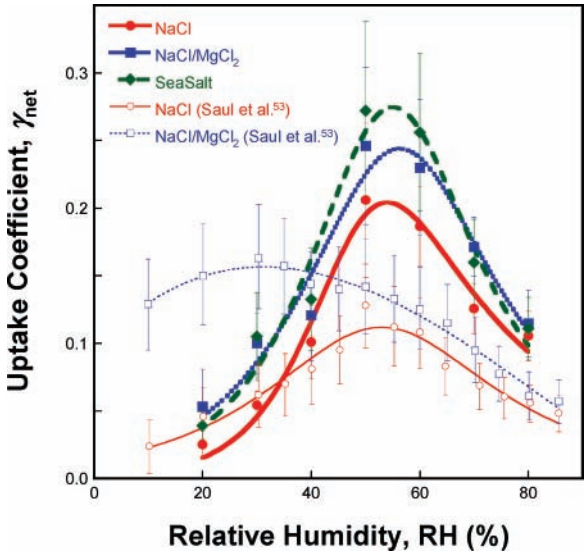

Figure 11. Values of initial uptake coefficient γ_{net} as a function of relative humidity for NaCl, mixture of NaCl/$MgCl_2$ ($X_{Mg/Na} = 0.114$) and sea salt particles. Solid symbols are experimental data of this work with $\bar{D}_p \sim 0.9$ μm. The open symbols represent data taken from Saul et al.[53] for deliquesced particles with $\bar{D}_d \sim 0.1$ μm. Lines are drawn to help show trends.

fortuitous because γ_{net} is particle-size dependent. For comparison, data from Saul et al.[53] ($\bar{D}_d \sim 0.1$ μm) are also included in the figure. The uptake coefficient initially increases with a decrease in RH, reaches its maximum at RH $\approx$ 55%, and then decreases as RH is further lowered. This behavior may be explained by considering the variation of chloride concentration. Over the RH range 55−80% a decrease in RH is accompanied by an increase in [Cl^-] in the droplets, leading to a larger reactive uptake, as predicted by eq 8. Below the efflorescence relative humidity (ERH $\approx$ 45%), the reactive uptake drops rapidly, but a sudden "shutoff" in reactivity was not observed. Rather, fairly considerable HNO_3 uptake onto NaCl particles was measured ($\gamma_{net} = 0.04-0.10$) under quite dry conditions (RH $\sim$ 30%). It is reasonable to expect that under this humidity there could still be trace amounts of surface absorbed water, which results in enhanced ionic mobility on the surface and subsequent replenishment of fresh NaCl onto the surface for further exposure.[55]

Comparison of NaCl to Sea Salt. Sea salt is a multicomponent inorganic salt. Besides the most abundant component, NaCl, it also contains magnesium salt constituents (e.g., $MgCl_2 \cdot 6H_2O$, $MgSO_4 \cdot H_2O$, $KMgCl_3 \cdot 6H_2O$). These minor constituents are more hygroscopic than NaCl.[104] Thermodynamic predictions[105] of the mineral sequences expected for evaporation of seawater indicate that magnesium salts are always crystallized last in the sequence as a result of their higher solubility. Therefore, dried sea salt particles have multilayered structure with the highest soluble and most abundant $MgCl_2$ salt at the top surface layer. In laboratory studies of heterogeneous aerosol reactions, NaCl is often used as a proxy for sea salt particles. To examine whether this is a good model for reactive uptake of real sea salt, we investigated HNO_3 uptake on a mixture of NaCl/$MgCl_2$ and sea salt particles with dry diameter of $\bar{D}_p = \sim 0.9$ μm. The results are shown in Figure 11. The dependency of γ_{net} on the relative humidity is similar for all three salts tested. Quantitatively, NaCl/$MgCl_2$ and sea salt take up HNO_3 more rapidly than NaCl does, though the differences among these samples are within margins of uncertainty. The apparent higher reactive uptake of HNO_3 is probably attributable to the following two factors. Higher [Cl^-]/[Na^+] ratios in both NaCl/$MgCl_2$ mixture and sea salt promote reactive uptake. Particles are in liquid form for RH > ERH. Reducing RH below ERH causes particles to crystallize. Albeit a nominally "solid" state, the small amount of highly hygroscopic magnesium salts remain liquid on the particle surface, which facilitates reactive gas uptake in the NaCl/$MgCl_2$ mixture and sea salt.[50,55] Similarly, it was recently reported that reactive uptake of N_2O_5 is enhanced on sea salt particles, as compared to NaCl particles.[54,103]

There are some qualitative discrepancies between the present work and that of Saul et al.[53] for NaCl/$MgCl_2$ particles at low humidity, as seen in Figure 11. The disagreements could arise from several differences between the two studies. The sea salt surface was reported to behave as a "saturated solution" with respect to the uptake and reaction of HNO_3.[106−108] At the onset of exposure to HNO_3 the uptake coefficient decreases invariably with the passage of time due to HNO_3 solubility and reaction with more hygroscopic component of sea salts, such as $MgCl_2$ in "saturated solution". The uptake coefficient levels off at a lower value after longer exposure. The time dependence is qualitatively consistent with SO_2 uptake onto sea salt particles.[109] In the work of Saul et al. the maximum exposure time was 10 s. For such a short period of reaction time HNO_3 reacts with the more soluble $MgCl_2$ in "saturated solution." The resulting uptake coefficient essentially measures the overall HNO_3 uptake onto the $MgCl_2$ solution. In contrast, exposure times greater than 8 min were applied in our study. Thus, over a large portion of the reaction period the surface $MgCl_2$ species were probably absent due to their consumption earlier in the reaction, leading to an overall reactive uptake onto sea salt particles. Therefore, the discrepancies could be caused by different time scales employed in the two studies. Also, the droplet size employed in the two studies differs by an order of magnitude. Thus, the different uptake behavior could be the result of different surface composition and morphology. Because neither information is available from the earlier study, the discussion above remains speculative and additional studies are required to resolve the discrepancy.

Particle Size Effect. Johnston and co-workers[52] reported that the HNO_3 reactive uptake on NaCl droplets increases linearly with the droplet diameter. Within the range of droplet diameters studied (0.1−0.23 μm), diffusion to/from the interface or reaction at the interface, mass accommodation at the gas−particle interface and HNO_3 solubility were concluded not to be the limiting factors for HNO_3 uptake. Rather, the uptake coefficient was limited by reaction rates within particles and, thus, closely follows the $\bar{D}_d$ dependency seen in eq 8—a conclusion that is quite reasonable for the droplet sizes studied. What was troubling is that when the data of Tolocka et al.[52] is extrapolated to 3 μm droplet, at which the uptake coefficient was reported by Abbatt and Waschewsky[45] to be >0.2, initial uptake continues to follow an apparent, linear dependency, increasing monotonically with an increase in the droplet diameter. For such a large uptake coefficient and considering that the droplet diameter is substantially larger than the mean free path of the gas, gaseous reactant diffusion to the droplet surface should play an important role. For example, taking the reactive uptake to be diffusion controlled with

$$\Gamma_g = \frac{8D_{HNO_3-N_2}}{D_d \bar{c}_{HNO_3}} \qquad (10)$$

we found that the uptake coefficient should eventually decease with an increase in droplet diameter. Thus, although a monotonic increase in the uptake coefficient with an increase in droplet size is expected for small particles, this trend cannot be

TABLE 4: Summary of Experimental Conditions (Series C) and Pseudo-First-Order Rate Constants[a]

$[HNO_3]_\infty$ (ppb)	$10^{-4}N_s$ (cm^{-2})	time (min)	$[Cl/Na]_t^{EDX}$	$[Cl/Na]_{t=0}^{EDX}$	$10^5\,k_I$ (s^{-1})
		Series C1: $\bar{D}_p = 0.57 \pm 0.05\ \mu m$			
3.6	1.9 ± 0.5	6	0.59 ± 0.20	0.96 ± 0.09	131 ($\times.9/\div2.7$)
3.6	1.9 ± 0.5	6	0.68 ± 0.27	0.99 ± 0.10	102 ($\times2.5/\div20.4$)
3.2	2.2 ± 0.5	5	0.75 ± 0.16	1.00 ± 0.10	93 ($\times2.0/\div4.2$)
3.2	3.6 ± 1.3	5	0.77 ± 0.13	0.99 ± 0.10	80 ($\times1.9/\div4.1$)
3.2	5.0 ± 1.3	5	0.82 ± 0.16	0.99 ± 0.10	60 ($\times2.4/\div b$)
3.2	6.8 ± 1.7	5	0.79 ± 0.13	0.99 ± 0.08	72 ($\times1.9/\div4.6$)
3.2	9.6 ± 2.4	5	0.84 ± 0.12	0.99 ± 0.07	53 ($\times2.1/\div b$)
2.0	32.5 ± 10.0	30	0.85 ± 0.17	1.00 ± 0.09	8.7 ($\times2.6/\div b$)
2.0	33.8 ± 8.2	30	0.94 ± 0.14	1.01 ± 0.07	3.6 ($\times3.8/\div b$)
2.0	35.6 ± 11.0	30	0.87 ± 0.14	0.97 ± 0.10	5.3 ($\times3.3/\div b$)
2.0	39.4 ± 1.1	30	0.89 ± 0.12	1.07 ± 0.07	9.9 ($\times1.9/\div4.6$)
2.0	42.5 ± 9.8	30	0.93 ± 0.12	1.04 ± 0.07	6.1 ($\times2.4/\div b$)
2.0	49.4 ± 18.0	30	0.95 ± 0.11	1.04 ± 0.09	4.7 ($\times2.8/\div b$)
		Series C2: $\bar{D}_p = 1.21 \pm 0.14\ \mu m$			
3.2	2.3 ± 0.6	15	0.98 ± 0.14	1.16 ± 0.06	19 ($\times2.0/\div6.8$)
3.2	3.8 ± 0.9	28	0.99 ± 0.10	1.17 ± 0.06	9.8 ($\times1.7/\div2.8$)
3.2	2.3 ± 0.6	30	1.03 ± 0.10	1.17 ± 0.06	7.0 ($\times1.9/\div5.7$)
3.2	4.8 ± 1.2	40	0.65 ± 0.20	1.16 ± 0.06	24 ($\times1.6/\div1.9$)
3.2	4.9 ± 1.2	35	0.77 ± 0.20	1.16 ± 0.06	19 ($\times1.8/\div2.4$)
2.0	24.4 ± 5.2	90	0.97 ± 0.21	1.15 ± 0.06	3.0 ($\times2.5/\div b$)
2.0	26.9 ± 4.9	90	1.03 ± 0.10	1.14 ± 0.06	1.9 ($\times2.2/\div b$)
2.5	24.4 ± 5.7	90	0.98 ± 0.12	1.14 ± 0.06	2.8 ($\times1.9/\div5.5$)
2.5	21.9 ± 4.9	90	0.94 ± 0.17	1.14 ± 0.06	3.4 ($\times2.1/\div b$)
2.5	23.8 ± 6.1	90	0.97 ± 0.16	1.14 ± 0.06	3.0 ($\times2.2/\div b$)
		Series C3: $\bar{D}_p = 1.70 \pm 0.04\ \mu m$			
2.7	1.0 ± 0.7	240	0.79 ± 0.24	1.19 ± 0.10	2.8 ($\times2.0/\div3.3$)
3.0	1.1 ± 1.0	180	0.88 ± 0.23	1.17 ± 0.05	2.6 ($\times2.1/\div6.0$)
3.0	1.5 ± 1.0	210	0.98 ± 0.30	1.19 ± 0.10	1.5 ($\times3.1/\div b$)
2.7	1.9 ± 0.9	240	0.88 ± 0.20	1.19 ± 0.10	2.0 ($\times2.0/\div4.1$)
2.7	2.7 ± 1.1	240	0.87 ± 0.17	1.19 ± 0.10	2.2 ($\times1.8/\div2.6$)
2.7	3.8 ± 0.7	240	0.79 ± 0.24	1.19 ± 0.10	2.8 ($\times1.9/\div3.2$)
3.2	4.3 ± 1.1	240	0.78 ± 0.29	1.19 ± 0.10	2.9 ($\times2.2/\div4.6$)
2.7	4.4 ± 0.9	240	0.88 ± 0.20	1.19 ± 0.10	2.1 ($\times1.9/\div3.7$)
3.0	5.0 ± 1.0	210	0.98 ± 0.30	1.19 ± 0.10	1.4 ($\times3.1/\div b$)
3.0	5.0 ± 1.0	180	0.88 ± 0.23	1.17 ± 0.05	2.6 ($\times2.1/\div5.6$)
2.7	5.0 ± 1.1	240	0.87 ± 0.17	1.19 ± 0.10	2.1 ($\times1.8/\div2.7$)

[a] All of the experiments were conducted at RH = 80%. Uncertainty values represent one standard deviation. k_I is the apparent pseudo-first-order rate constant of chloride loss, determined from eq 5, and the uncertainty factors in parentheses correspond to ± one standard deviation in $[Cl/Na]_t^{EDX}$ and $[Cl/Na]_{t=0}^{EDX}$. [b] The lower limit cannot be determined because of the small extent of reaction; i.e., the lower uncertainty limit is given by zero extent of reaction.

satisfactorily explained over a wide range of particle sizes within the realm of a resistance model of sequential gaseous reactant diffusion, mass accommodation, dissolution and reaction.[74] This is particularly true for particles with diameter substantially larger than the mean free path of the gas.

To provide better insight into the variation of reactive uptake as a function of droplet size and expand the available dataset, we determined the uptake coefficient as a function of droplet diameter from 1 to 3.6 μm under RH = 80%. Table 4 lists of the kinetic data measured for this series of experiments. Figure 12 presents the values of the uptake coefficient as a function of droplet diameter. Literature data[45,52,53] are also included for comparison. The variation of the uptake coefficient from the present work differs qualitatively from those of Johnston and co-workers.[52] In the range of droplet size studied, γ_{net} decreases monotonically with an increase in droplet size. Taking these data together reveals a characteristic rise-then-fall behavior, which is in fact expected by considering the various kinetic and diffusion effects. Specifically, we make use of the resistance model,[74] in which the overall net uptake coefficient is expressed in terms of the sum of resistances corresponding to a number of sequential and parallel processes,

$$\frac{1}{\gamma_{net}} = \frac{1}{\Gamma_g} + \frac{1}{\alpha} + \frac{1}{(\Gamma_{sol} + \Gamma_{rxn})} + \frac{1}{\Gamma_d} \qquad (11)$$

In the above expression $1/\Gamma_g$, $1/\alpha$, $1/\Gamma_{sol}$, $1/\Gamma_{rxn}$, and $1/\Gamma_d$ represent the resistances to reaction due to gaseous reactant diffusion, mass accommodation, HNO_3 dissolution in the droplet, chemical reaction in the condensed-phase and aqueous-phase diffusion, respectively. Under the condition of the current study where the exposure time is relatively long, eq 11 is only approximate because of changes expected in chemical composition of the droplet as the reaction proceeds. Nonetheless, the equation is useful for understanding the rate-limiting processes during HNO_3 uptake.

It is known that α does not substantially contribute to overall uptake.[52,53] It is also reported that $1/\Gamma_{sol}$ is insignificant relative to $1/\gamma_{net}$ in the flow reactor study with maximum exposure time of 10 s. It has been previously shown[74] that Γ_{sol} can be expressed as

$$\Gamma_{sol} = \frac{4HRT}{\bar{c}_{HNO_3}}\sqrt{\frac{D_l}{\pi t}} \qquad (12)$$

where H is Henry's law constant, D_l is the aqueous-phase diffusion coefficient, and t is the contact time between HNO_3 and the droplet. All our experiments have exposure times longer than 5 min. For t = 10 min, Γ_{sol} is approximately 0.05, which indicates HNO_3 dissolution to be unimportant, as will be discussed below.

Excluding the contribution of aqueous-phase diffusion for the time being, eq 11 can be reduced to

$$\frac{1}{\gamma_{net}} = \frac{1}{\Gamma_{rxn} + \Gamma_{sol}} + \frac{1}{\Gamma_g} \quad (13)$$

where

$$\Gamma_{rxn} = \frac{4k_{II}^*[Cl^-]_d D_d}{3\bar{c}_{HNO_3}} \quad (14)$$

and the expressions for Γ_{sol} and Γ_g have already been given. In eq 14, k_{II}^* is an intrinsic, second-order rate constant of the gas-surface reaction without being influenced by gaseous diffusion. By using k_{II}^* as a single adjustable variable and fitting the γ_{net} value of Saul et al.,[53] we obtain a prediction by the simplified model (11), shown as the dark solid line in Figure 12. Also, k_{II}^* was found to be 1×10^{-13} cm^3 molecule^{-1} s^{-1}, which is considerably smaller than the collision limit. Because the dissolution of HNO_3 on deliquesced particle is expected to be rapid, this k_{II}^* value would indicate that for the smaller droplets studied previously[52,53] the reactive HNO_3 uptake might be limited by HCl formation in the droplet, a finding consistent with the conclusion reached previously.[52] Using $k_{II}^* = 1 \times 10^{-13}$ cm^3 molecule^{-1} s^{-1}, we find Γ_{rxn} to be unity for a 2 μm droplet, which is substantially larger than the Γ_{sol} value estimated earlier. For this reason Γ_{sol} was excluded from the analysis.

The simple model (13) captures, for the most part, the characteristic dependence of γ_{net} on the droplet diameter. For larger particles the slightly larger deviation may be caused by aqueous-phase diffusion of the chloride ion, which is not considered in eq 13. It has been shown in the study of reactive uptake of ozone by oleic acid aerosols[110] that aqueous-phase oleic acid diffusion plays an important role in the decrease of uptake coefficient with increasing size. Because NO_3^- is physically larger than Cl^- and it also has a larger polarizability than Cl^-, it probably has a higher propensity to stay at the interface. This speculation is consistent with recent findings that the Br^- ion tends to migrate to the surface in seawater.[111,112] The tendency of NO_3^- to stay at the interface would inhibit Cl^- diffusion to replenish its concentration at the interfacial layer to some extent. The effect should be more appreciable for larger droplets.

Regardless, the combined experimental and modeling results shown in Figure 12 clearly demonstrate that finite rate reaction kinetics is the major contributor to reactive uptake for droplet diameter below 0.7 μm and gaseous diffusion becomes a limiting factor of HNO_3 uptake in addition to aqueous diffusion for larger droplets. Thus, the current analysis is consistent with the conclusion of Johnston and co-workers,[52,53] that their data fall in the kinetic-controlled region. Another interesting conclusion from the current study is that the peak uptake coefficient occurs immediately below the size at which sea salt aerosols begin to contribute notably to light scattering and backscattering.

Our conclusion that the uptake is diffusion controlled for droplets larger than 0.7 μm is consistent with the findings of Abbatt and Waschewsky,[45] even though their reported uptake coefficient is considerably larger than the value reported here for a comparable droplet size. In that study the uptake coefficient was measured somewhat indirectly by following the disappearance of vapor-phase HNO_3 by chemical ionization mass spectrometry. The HNO_3 concentration employed was substantially higher than those of the current study. It is possible that some of the nitric acid is consumed by secondary reactions in the flow reactor, leading to an artificially large uptake coefficient.

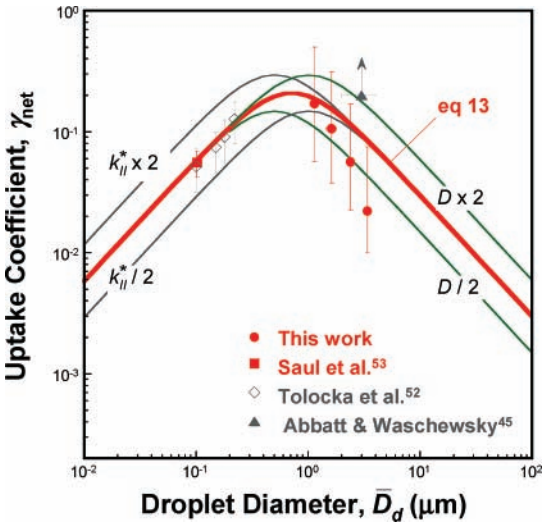

Figure 12. Experimental values of γ_{net} under RH = 80% as a function of droplet diameter. Key: symbols, experimental data; dark solid line, eq 13 without considering Γ_{sol} ($k_{II}^* = 10^{-13}$ cm^3 molecules^{-1} s^{-1}, $D_{HNO_3-N_2} = 0.118$ cm^2/s). The original data of Tolocka et al.[52] are in error due to a systematic measurement problem for the gas-phase HNO_3.[53] These data are multiplied by a factor of 10 to match the more recent datum of Saul et al. The data point reported by Abbatt and Waschewsky[45] is the lower-limit under 75% RH over a droplet diameter of 2−4 μm.

Last, it is important to note that the characteristic rise-then-fall behavior of γ_{net} exhibited in Figure 12 is expected for a large number of heterogeneous aerosol reactions. Sensitivities to kinetic rate and diffusivity variations are presented in the figure. The position of the peak is clearly dependent on the details of the reaction kinetics and diffusivity. We previously used a similar technique and determined the uptake coefficient of $^{\bullet}$OH to be >0.1 on deliquesced NaCl droplets 1.8 μm in diameter under RH = 80%.[86] This uptake coefficient was not corrected for half-sphere diffusion; thus, it is likely to be a factor of ~2 lower than it should be. Because the intrinsic reaction of $^{\bullet}$OH with NaCl is known to be fast and molecular dynamics simulations show that the uptake coefficient can be as large as 0.83,[113,114] the uptake at that droplet size must also be diffusion controlled. Using an $^{\bullet}$OH diffusivity of 0.33 cm^2/s and eq 13, we obtained a γ_{net} value of ~0.2, which is in close agreement with the substrate-based experiment upon a factor of 2 correction, as discussed above.

Significance and Limitations of the Method. A majority of methodologies and techniques used to study heterogeneous reaction kinetics of atmospheric relevance monitor changes in the gas-phase concentrations, whereas measurements of the solid phase are typically used to provide fundamental, albeit rather qualitative, information about reaction mechanisms. Several recent review articles[3,6,115] about aerosol heterogeneous chemistry have markedly specified the need for development of experimental methodologies to measure uptake on isolated particles and not bulk powders or solids to remove uncertainties inherent to bulk sample measurements.[6] With an increased recognition of the need to understand and quantify changes in individual particles due to their atmospheric reactions, more attention is being given now to the application of single particle analysis techniques to study kinetics of gas-to-particle reac-

tions.[52,53,86,116,117] One specific recommendation from these reviews is that laboratory studies should also capture realistic atmospheric conditions of relative humidity, temperature, pressure, reaction time, and trace reactive gas concentrations relevant to the atmosphere. For example, this and many other studies have demonstrated that water plays an important role that can fundamentally affect the kinetics and mechanisms of atmospheric gas-to-particle reactions. There are many more gas-phase components that might be similarly influential in heterogeneous aerosol chemistry. For instance, recently Shaka et al.[118] demonstrated that the reaction of gaseous OH with chloride ions can modulate sea salt alkalinity and enhance the uptake and oxidation of SO_2 by sea salt aerosol.

Application of the presented PS-SFR experimental approach for laboratory studies of atmospheric gas-to-particle chemistry is fairly straightforward because it can provide many of the realistic atmospheric conditions previously mentioned. In addition, the approach can be used for studies of heterogeneous atmospheric chemistry of field collected particles, and particles after sequential exposures to different reactive gases and their mixtures. This novel approach is well suited for applications in surface science and chemical catalysis studies. The key requirements are that the substrate reactivity is small compared to that of the deposited particles and that chemical changes in the particles can be followed quantitatively in response to the reaction.

Several details of the experiment and data analysis are worthy of further discussion: (a) the effect of substrate reactivity, (b) the limited range of the reaction extent that can be detected and used for kinetic analysis and (c) estimation of particle size and morphology. As to the first issue, the underlying assumption of the experiment is that the substrate is uncreative, i.e., HNO_3 consumption by the substrate does not affect kinetics of the HNO_3-to-NaCl reaction ($\delta k_s \ll 1$ in eq 7). If some of the reactive gas molecules are removed by the substrate, values of k_I and γ_{net} would be underestimated. Hence, as discussed in this manuscript and in our earlier publication,[86] a rigorous view of the uptake coefficients reported here is that they represent only the lower limits. Thus, our approach will be the most useful for cases where the particles are highly reactive. It is also important to note that although the exact reactivity of the substrate is not known, its relative inertness with respect to the HNO_3-to-NaCl reaction is clearly inferred from the rise of the $[HNO_3]/k_I$ values at high particle density N_s, as seen in Figure 10. This dependence of k_I on N_s would not have been observed if the reaction kinetics was limited by the substrate reactivity.

The reaction extent that can be measured and then used for kinetic analysis is limited to a fairly narrow range. First, the CCSEM/EDX method of analysis is not sensitive enough to detect less than ~10% of the reaction extent. On the other hand, an inherent assumption adopted for the data analysis of this study is that we use the initial chlorine concentration for calculations of the uptake coefficient ($[Cl^-]_{d,0} = 5$ M, eq 9), while the chlorine concentration is constantly decreasing as the reaction proceeds. To keep our experimental data as close to this assumption as possible, we conducted almost all of the experiments under conditions with the reaction extent being limited to <30%. Again, given that the chloride concentration in eq 9 is overestimated, the value derived for γ_{net} represents a lower limit for the reaction probability.

In the case of substrate-deposited particles, calculation of their surface areas (S_d in eq 8) available for reaction requires knowledge of the particle morphology. Supported by a number of microscopic studies indicating that a freshly deliquesced NaCl and sea salt particles are well-approximated by a sphere tangent to the substrate,[85,119,120] we used the perfect sphere approximation throughout this work. In our previous study of heterogeneous reaction of NaCl with OH radicals,[86] however, we found that SEM images taken after the reaction showed a halo of residue around each vacuum-dried particle, indicating that during the reaction NaCl droplets wetted the substrate and spread to approximately twice its spherical wet diameter. We assessed the magnitude of this effect on the surface area available for the reaction by considering the reacted particle as a spherical cap with volume equal to that of a sphere. We estimated that the surface area of a spherical cap was only a factor of 1.3 larger than that of a perfect sphere.[86] Wetting the substrate and spreading of the particle contour in that study was likely due to the formation of a highly hygroscopic mixture of NaOH and NaOCl as the reaction products.[79] In contrast, thorough inspection of the SEM images of this study indicated no evidence of such an effect. This might be just a coincidence because dry density and hygroscopic growth factors of NaCl and $NaNO_3$ particles are almost identical at 80% RH.[97,121,122] Therefore, sizes of particles studied in this work are generally not expected to be altered considerably during the reaction. Regardless, uncertainty introduced by particle morphology is less significant compared to the overall uncertainty of composition measurements.

Conclusions

Heterogeneous reaction kinetics of gaseous nitric acid with deliquesced sodium chloride, $NaCl/MgCl_2$ mixture (representative of sea salt) and sea salt particles were investigated with a novel particle-on-substrate stagnation flow reactor (PS-SFR) experimental approach. Particles deposited on a TEM grid are exposed to gaseous HNO_3 by impingement of an axisymmetric gas jet under conditions, including particle size, relative humidity, and reaction time, relevant to the atmospheric chemistry of sea salt particles. Chemical composition of particles is measured with the CCSEM/EDX technique. Computational fluid dynamics simulations were carried out to ensure optimal operation of the particle exposure experiments and assess the influence of several key reactor parameters on the uniformity of reaction across the particles deposited surface. The optimal reactor parameters were implemented in the reactor design and operation.

Three series of experiments were conducted in which the particle loading, free stream HNO_3 concentration, reaction time, particle size, and relative humidity were varied for one or more types of salt particles. The first series of experiments was conducted for $\bar{D}_p = 0.8$ μm particles under 80% relative humidity with the objective to assess the role of diffusion-kinetic coupling arising from competition for gaseous HNO_3 among adjacent droplets on the TEM grid surface. Results show that the variation of the apparent, pseudo-first-order rate constant with particle loading and HNO_3 concentration in the free stream is entirely consistent with a diffusion-kinetic analysis previously reported.[86] Extrapolation of the data to the low particle density limit yielded an intrinsic, second-order rate constant $k_{II} = 5.7 \times 10^{-15}$ cm^3 molecule^{-1} s^{-1}. Under the same condition the initial, net reaction uptake coefficient was found to be $\gamma_{net} = 0.11$ with an uncertainty factor of 3.

An additional series of experiments examined the variations of HNO_3 uptake on pure NaCl, a sea salt-like mixture of NaCl and $MgCl_2$ (Mg-to-Cl molar ration of 0.114) and real sea salt particles as a function of relative humidity. For three types of salt particles, all with $\bar{D}_p \sim 0.9\ \mu m$, behavior of the uptake coefficient is similar over the relative humidity range 20−80%. The uptake was found to peak around a relative humidity of 55% with γ_{net} well over 0.2 for sea salt. Below the efflorescence relative humidity the uptake coefficient decreases rapidly without a sudden extinction in reactivity. Due to the higher hygroscopicity of magnesium salt, the uptake of HNO_3 on sea salt particles was more rapid than that on the mixture of NaCl and $MgCl_2$, and uptake on both sea salt and sea salt-like mixture was faster than on pure NaCl.

The uptake of HNO_3 on pure NaCl particles was also examined over the particle size range of $0.57 \leq \bar{D}_p \leq 1.7\ \mu m$ ($1.1 \leq \bar{D}_d \leq 3.4\ \mu m$). Under a constant relative humidity of 80% the uptake coefficient decreased monotonically with an increase in particle size. Application of a resistance model implementing reaction kinetics and gas-phase diffusion over a single particle suggests that, over the range of particle size studied, the uptake is largely controlled by gaseous reactant diffusion from the free stream to the particle surface. A combined consideration of uptake coefficients obtained in the present study and those previously reported for substantially smaller droplets ($\bar{D}_d \sim 0.1-0.23\ \mu m$)[52,53] indicate that the uptake coefficient follows a characteristic rise-then-fall behavior with respect to droplet size and that the peak reactivity of HNO_3 with NaCl occurs at a droplet diameter of $\sim 0.7\ \mu m$.

Last, we note that sea salt particles of micron size are ubiquitous in and near the marine boundary layer. They are responsible for a large fraction of light scattering and back-scattering.[123] These micron-size particles are, however, too large to be efficiently transmitted to single-particle mass spectrometers (SPMS) commonly used to detect chloride depletion. In addition, the fact that the particles must be suspended in a gas requires the reaction to take place in a flow reactor for no longer than tens of seconds, far shorter than the lifetime of typical sea salt particles in atmospheric chemistry. For these reasons reactions of micron-size particles are not "accessible" by FR-SPMS. However, the PS-SFR experiment coupled with the CCSEM/EDX technique adopted here allows the particles to undergo exposure to a reactive gas over a considerably longer period of time and is well suited for particles of micron size. The technique also offers options for multi-instrumental microanalysis and is applicable to both laboratory generated and field collected samples. It should be noted that this approach does have one important limitation: particles smaller than 0.5 μm may not be accurately probed because of the potential damage caused from the electron beam.[80] These considerations lead us to believe that a combination of FR-SPMS and PS-SFR/CCSEM/EDX would be essential to understand uptake over a wide range of particle sizes and experimental conditions.

Acknowledgment. The work was supported by Tropospheric Chemistry and Radiation Sciences programs at the National Aeronautics and Space Administration (grant numbers NNG06GE89G and NNG06GI51G). The experimental part of this work was performed at the William R. Wiley Environmental Molecular Sciences Laboratory, a national scientific user facility sponsored by the Department of Energy's Office of Biological and Environmental Research and located at Pacific Northwest National Laboratory (PNNL). PNNL is operated by the U.S. Department of Energy by Battelle Memorial Institute under contract No. DE-AC06-76RL0 1830.

Supporting Information Available: Seven plots indicating variations of $[HNO_3]/k_I$ as a function of reaction time for seven fixed values of particle number on the substrate (N_s) (Figure S1). Values of $1/k_I$ as a function of particle number density on the substrate surface (N_s), determined experimentally from Cl depletion, N and O enhancements for the three series of experiments (Figure S2). This material is available free of charge via the Internet at http://pubs.acs.org.

References and Notes

(1) Ravishankara, A. R. *Science* **1997**, *276*, 1058.
(2) Andreae, M. O.; Crutzen, P. J. *Science* **1997**, *276*, 1052.
(3) Finlayson-Pitts, B. J. *Chem. Rev.* **2003**, *103*, 4801.
(4) Finlayson-Pitts, B. J.; Pitts, J. N., Jr. *Science* **1997**, *276*, 1045.
(5) Rossi, M. J. *Chem. Rev.* **2003**, *103*, 4823.
(6) Usher, C. R.; Michel, A. E.; Grassian, V. H. *Chem. Rev.* **2003**, *103*, 4883.
(7) Abbatt, J. P. D. *Chem. Rev.* **2003**, *103*, 4783.
(8) Rudich, Y. *Chem. Rev.* **2003**, *103*, 5097.
(9) Charlson, R. J.; Schwartz, S. E.; Hales, J. M.; Cess, R. D.; Coakley, J. A.; Hansen, J. E.; Hofmann, D. J. *Science* **1992**, *255*, 423.
(10) Pilinis, C.; Pandis, S. N.; Seinfeld, J. H. *J. Geophys. Res. Atmos.* **1995**, *100*, 18739.
(11) Baker, M. B. *Science* **1997**, *276*, 1072.
(12) Pandis, S. N.; Wexler, A. S.; Seinfeld, J. H. *J. Phys. Chem.* **1995**, *99*, 9646.
(13) Schwartz, S. E. *J. Aerosol Sci.* **1996**, *27*, 359.
(14) Penner, J. E.; Charlson, R. J.; Hales, J. M.; Laulainen, N. S.; Leifer, R.; Novakov, T.; Ogren, J.; Radke, L. F.; Schwartz, S. E.; Travis, L. *Bull. Am. Meteor. Soc.* **1994**, *75*, 375.
(15) Penner, J. E.; Dickinson, R. E.; Oneill, C. A. *Science* **1992**, *256*, 1432.
(16) Chow, J. C.; Bachmann, J. D.; Wierman, S. S. G.; Mathai, C. V.; Malm, W. C.; White, W. H.; Mueller, P. K.; Kumar, N.; Watson, J. G. *J. Air Waste Manage. Assoc.* **2002**, *52*, 973.
(17) Malm, W. C.; Molenar, J. V. *J. Air Pollut. Control Assoc.* **1984**, *34*, 899.
(18) Dockery, D. W.; Pope, C. A.; Xu, X. P.; Spengler, J. D.; Ware, J. H.; Fay, M. E.; Ferris, B. G.; Speizer, F. E. *New England J. Med.* **1993**, *329*, 1753.
(19) Pope, C. A.; Burnett, R. T.; Thun, M. J.; Calle, E. E.; Krewski, D.; Ito, K.; Thurston, G. D. *J. Am. Med. Assoc.* **2002**, *287*, 1132.
(20) Pope, C. A.; Dockery, D. W.; Schwartz, J. *Inhal. Toxicol.* **1995**, *7*, 1.
(21) Pope, C. A.; Thun, M. J.; Namboodiri, M. M.; Dockery, D. W.; Evans, J. S.; Speizer, F. E.; Heath, C. W. *Am. J. Respir. Crit. Care Med.* **1995**, *151*, 669.
(22) Pope, C. A.; Verrier, R. L.; Lovett, E. G.; Larson, A. C.; Raizenne, M. E.; Kanner, R. E.; Schwartz, J.; Villegas, M.; Gold, D. R.; Dockery, D. W. *Am. Heart J.* **1999**, *138*, 890.
(23) Keene, W. C.; Sander, R.; Pszenny, A. A. P.; Vogt, R.; Crutzen, P. J.; Galloway, J. N. *J. Aerosol Sci.* **1998**, *29*, 339.
(24) Robbins, R. C.; Cadle, R. D.; Eckhardt, D. L. *J. Meteor.* **1959**, *16*, 53.
(25) Cadle, R. D.; Robbins, R. C. *Discuss. Faraday Soc.* **1960**, 155.
(26) Schroede, Wh; Urone, P. *Environ. Sci. Technol.* **1974**, *8*, 756.
(27) Cicerone, R. J. *Rev. Geophys.* **1981**, *19*, 123.
(28) Zetzsch, C.; Behnke, W. *Ber. Bunsen-Ges. Phys. Chem.-Phys. Chem. Chem. Phys* **1992**, *96*, 488.
(29) Behnke, W.; Zetzsch, C. *J. Aerosol Sci.* **1989**, *20*, 1167.
(30) Behnke, W.; Nolting, F.; Zetzsch, C. *J. Aerosol Sci.* **1987**, *18*, 65.
(31) Zetzsch, C.; Pfahler, G.; Behnke, W. *J. Aerosol Sci.* **1988**, *19*, 1203.
(32) Behnke, W.; Kruger, H. U.; Scheer, V.; Zetzsch, C. *J. Aerosol Sci.* **1991**, *22*, S609.
(33) Behnke, W.; George, C.; Scheer, V.; Zetzsch, C. *J. Geophys. Res. Atmos.* **1997**, *102*, 3795.
(34) Leu, M. T.; Timonen, R. S.; Keyser, L. F. *J. Phys. Chem. A* **1997**, *101*, 278.
(35) Leu, M. T.; Timonen, R. S.; Keyser, L. F.; Yung, Y. L. *J. Phys. Chem.* **1995**, *99*, 13203.
(36) Laux, J. M.; Hemminger, J. C.; Finlayson-Pitts, B. J. *Geophys. Res. Lett.* **1994**, *21*, 1623.
(37) Finlayson-Pitts, B. J. *Nature* **1983**, *306*, 676.
(38) Fenter, F. F.; Rossi, M. J. *J. Phys. Chem.* **1996**, *100*, 13765.

(39) Caloz, F.; Fenter, F. F.; Rossi, M. J. *J. Phys. Chem.* **1996**, *100*, 7494.
(40) Fenter, F. F.; Caloz, F.; Rossi, M. J. *J. Phys. Chem.* **1996**, *100*, 1008.
(41) Seisel, S.; Caloz, F.; Fenter, F. F.; van den Bergh, H.; Rossi, M. J. *Geophys. Res. Lett.* **1997**, *24*, 2757.
(42) Caloz, F.; Seisel, S.; Fenter, F. F.; Rossi, M. J. *J. Phys. Chem. A* **1998**, *102*, 7470.
(43) Davies, J. A.; Cox, R. A. *J. Phys. Chem. A* **1998**, *102*, 7631.
(44) ten Brink, H. M. *J. Aerosol Sci.* **1998**, *29*, 57.
(45) Abbatt, J. P. D.; Waschewsky, G. C. G. *J. Phys. Chem. A* **1998**, *102*, 3719.
(46) Behnke, W.; Elend, M.; Krüger, U.; Zetzsch, C. *J. Atmos. Chem.* **1999**, *34*, 87.
(47) Koch, T. G.; van den Bergh, H.; Rossi, M. J. *Phys. Chem. Chem. Phys.* **1999**, *1*, 2687.
(48) Finlayson-Pitts, B. J.; Johnson, S. N. *Atmos. Environ.* **1988**, *22*, 1107.
(49) Finlayson-Pitts, B. J.; Livingston, F. E.; Berko, H. N. *Nature* **1990**, *343*, 622.
(50) Ghosal, S.; Hemminger, J. C. *J. Phys. Chem. A* **1999**, *103*, 4777.
(51) Guimbaud, C.; Arens, F.; Gutzwiller, L.; Gaggeler, H. W.; Ammann, M. *Atmos. Chem. Phys.* **2002**, *2*, 249.
(52) Tolocka, M. P.; Saul, T. D.; Johnston, M. V. *J. Phys. Chem. A* **2004**, *108*, 2659.
(53) Saul, T. D.; Tolocka, M. P.; Johnston, M. V. *J. Phys. Chem. A* **2006**, *110*, 7614.
(54) Thornton, J. A.; Abbatt, J. P. D. *J. Phys. Chem. A* **2005**, *109*, 10004.
(55) Finlayson-Pitts, B. J.; Hemminger, J. C. *J. Phys. Chem. A* **2000**, *104*, 11463.
(56) Erickson, D. J.; Seuzaret, C.; Keene, W. C.; Gong, S. L. *J. Geophys. Res. Atmos.* **1999**, *104*, 8347.
(57) Khalil, M. A. K.; Moore, R. M.; Harper, D. B.; Lobert, J. M.; Erickson, D. J.; Koropalov, V.; Sturges, W. T.; Keene, W. C. *J. Geophys. Res. Atmos.* **1999**, *104*, 8333.
(58) Keene, W. C.; Khalil, M. A. K.; Erickson, D. J.; McCulloch, A.; Graedel, T. E.; Lobert, J. M.; Aucott, M. L.; Gong, S. L.; Harper, D. B.; Kleiman, G.; Midgley, P.; Moore, R. M.; Seuzaret, C.; Sturges, W. T.; Benkovitz, C. M.; Koropalov, V.; Barrie, L. A.; Li, Y. F. *J. Geophys. Res. Atmos.* **1999**, *104*, 8429.
(59) Sander, R.; Keene, W. C.; Pszenny, A. A. P.; Arimoto, R.; Ayers, G. P.; Baboukas, E.; Cainey, J. M.; Crutzen, P. J.; Duce, R. A.; Honninger, G.; Huebert, B. J.; Maenhaut, W.; Mihalopoulos, N.; Turekian, V. C.; Van Dingenen, R. *Atmos. Chem. Phys.* **2003**, *3*, 1301.
(60) Junge, C. E. *Tellus* **1956**, *8*, 127.
(61) Moyers, J. L.; Duce, R. A. *J. Geophys. Res.* **1972**, *77*, 5330.
(62) Martens, C. S.; Wesolows, J.; Harriss, R. C.; Kaifer, R. *J. Geophys. Res.* **1973**, *78*, 8778.
(63) Prospero, J. M.; Charlson, R. J.; Mohnen, V.; Jaenicke, R.; Delany, A. C.; Moyers, J.; Zoller, W.; Rahn, K. *Rev. Geophys.* **1983**, *21*, 1607.
(64) Mouri, H.; Okada, K. *Geophys. Res. Lett.* **1993**, *20*, 49.
(65) Graedel, T. E.; Keene, W. C. *Global Biogeochem. Cyc.* **1995**, *9*, 47.
(66) Zhuang, H.; Chan, C. K.; Fang, M.; Wexler, A. S. *Atmos. Environ.* **1999**, *33*, 4223.
(67) Hoffman, R. C.; Gebel, M. E.; Fox, B. S.; Finlayson-Pitts, B. J. *Phys. Chem. Chem. Phys.* **2003**, *5*, 1780.
(68) Laux, J. M.; Fister, T. F.; Finlayson-Pitts, B. J.; Hemminger, J. C. *J. Phys. Chem.* **1996**, *100*, 19891.
(69) Sporleder, D.; Ewing, G. E. *J. Phys. Chem. A* **2001**, *105*, 1838.
(70) Beichert, P.; FinlaysonPitts, B. J. *J. Phys. Chem.* **1996**, *100*, 15218.
(71) Peters, S. J.; Ewing, G. E. *J. Phys. Chem. B* **1997**, *101*, 10880.
(72) Peters, S. J.; Ewing, G. E. *Langmuir* **1997**, *13*, 6345.
(73) Allen, H. C.; Laux, J. M.; Vogt, R.; Finlayson-Pitts, B. J.; Hemminger, J. C. *J. Phys. Chem.* **1996**, *100*, 6371.
(74) Finlayson-Pitts, B. J.; Pitts, J. N., Jr. *Chemistry of the Upper and Lower Atmosphere*; Academic Press: San Diego 2000.
(75) Seinfeld, J. H.; Pandis, S. N. *Atmospheric Chemistry and Physics*; John Wiley & Sons: New York, 1998.
(76) Clarke, A. D.; Davis, D.; Kapustin, V. N.; Eisele, F.; Chen, G.; Paluch, I.; Lenschow, D.; Bandy, A. R.; Thornton, D.; Moore, K.; Mauldin, L.; Tanner, D.; Litchy, M.; Carroll, M. A.; Collins, J.; Albercook, G. *Science* **1998**, *282*, 89.
(77) Wash, C. H.; Davidson, K. L.; Jordan, D. S. *Geoscience and Remote Sensing Symposium*, 1995. *IGARSS '95. 'Quantitative Remote Sensing for Science and Applications', International*.
(78) Krueger, B. J.; Grassian, V. H.; Laskin, A.; Cowin, J. P. *Geophys. Res. Lett.* **2003**, *30*, 1148. doi:10.1029/2002GL016563.
(79) Laskin, A.; Gaspar, D. J.; Wang, W.; Hunt, S. W.; Cowin, J. P.; Colson, S. D.; Finlayson-Pitts, B. J. *Science* **2003**, *301*, 340.
(80) Hoffman, R.C.; Laskin, A.; Finlayson-Pitts, B. J. *J. Aerosol Sci.* **2004**, *35* (7), 869.
(81) Krueger, B. J.; Grassian, V. H.; Iedema, M. J.; Cowin, J. P.; Laskin, A. *Anal. Chem.* **2003**, *75*, 5170.
(82) Krueger, B. J.; Grassian, V. H.; Cowin, J. P.; Laskin, A. *Atmos. Environ.* **2004**, *38*, 6253. Erratum published in *Atmos. Environ.* **2005**, *39*, 395.
(83) Laskin, A.; Wietsma, T.W.; Krueger, B. J.; Grassian, V. H. *J. Geophys. Res.*−*Atmos.* **2005**, *110*, D10106. doi:10.1029/2004JD005469.
(84) Zuberi, B.; Johnson, K. S.; Aleks, G. K.; Molina, L. T.; Molina, M. J.; Laskin, A. *Geophys. Res. Lett.* **2005**, *32*, L01807. doi:10.1029/2004GL021496.
(85) Laskin, A.; Cowin, J. P.; Iedema, M. J. *J. Electron Spectrosc. Relat. Phenom.* **2006**, *150*, 260.
(86) Laskin, A.; Wang, H.; Robertson, W. H.; Cowin, J. P.; Ezell, M. J.; Finlayson-Pitts, B. J. *J. Phys. Chem. A* **2006**, *110*, 10619.
(87) Neuman, J. A.; Huey, L. G.; Ryerson, T. B.; Fahey, D. W. *Environ. Sci. Technol.* **1999**, *33*(7), 1133.
(88) Hua, Y. N. *J. Trace Microprobe Technol.* **2003**, *21*, 25.
(89) Hering, S. V.; Lawson, D. R.; Allegrini, I.; Febo, A.; Perrino, C.; Possanzini, M.; Sickles, J. E., I.; Anlauf, K. G.; Wiebe, A.; Appel, B. R.; John, W.; Ondo, J.; Wall, S.; Braman, R. S.; Sutton, R.; Cass, G. R.; Solomon, P. A.; Eatough, D. J.; Eatough, N. L.; Ellis, E. C.; Grosjean, D.; Hicks, B. B.; Womack, J. D.; Horrocks, J.; Knapp, K. T.; Ellestad, T. G.; Paur, R. J.; Mitchell, W. J.; Pleasant, M.; Peake, E.; MacLean, A.; Pierson, W. R.; Brachaczek, W.; Schiff, H. I.; Mackay, G. I.; Spicer, C. W.; Stedman, D. H.; Winer, A. M.; Biermann, H. W.; Tuazon, E. C. *Atmos. Environ.* **1988**, *22*, 1519.
(90) Schlichting, H. *Boundary-Layer Theory*; McGraw-Hill: New York 1968.
(91) Phares, D. J.; Smedley, G. T.; Flagan, R. C. *Phys. Fluids* **2000**, *12*, 2046.
(92) *Fluent 6.2 User's Guide*; Fluent Inc.: Lebanon, NH, 2005.
(93) Hirschfelder, J. O.; Curtiss, C. F.; Bird, R. B. *Molecular Theory of Gases and Liquids*; John Wiley & Sons: New York 1966.
(94) Turns, S. *An Introduction to Combustion*; McGraw-Hill: New York 2000.
(95) Yaws, C. *Chemical Properties Handbook: Physical, Thermodynamics, Environmental Transport, Safety and Health Related Properties for Organic and Inorganic Chemical*; McGraw-Hill: New York 1998.
(96) Poling, B. E.; Prausnitz, J. M.;O'Connell, J. O. *The Properties of Gases and Liquids*; McGraw-Hill: New York 2000.
(97) Tang, I. N. *J. Geophys. Res. Atmos.* **1997**, *102*, 1883.
(98) van Doren, J. M.; Watson, L. R.; Kolb, C. E. *J. Phys. Chem.* **1990**, *94*, 3265.
(99) Kirchner, W.; Welter, F.; Bongartz, A.; Kames, J.; Schweignoefer. S.; Schurath. U. *J. Atmos. Chem.* **1990,** *10*, 427.
(100) Ponche, J. L.; George, C.; Mirabel, P. *J. Atmos. Chem.* **1993**, *16*, 1.
(101) Schutze, M.; Herrmann, H. *Phys. Chem. Chem. Phys.* **2002**, *4*, 60.
(102) Thornton, J. A.; Braban, C. F.; Abbatt, J. P. D. *Phys. Chem. Chem. Phys.* **2003**, *5*, 4593.
(103) Stewart, D. J.; Griffiths, P. T.; Cox, R. A. *Atmos. Chem. Phys.* **2004**, *4*, 1381.
(104) Lide, D. R., Ed. *CRC Handbook of Chemistry and Physics*, 63rd ed.; CRC Press: Boca Raton, FL, 1983. (Solubilities of $MgCl_2 \cdot 6H_2O$, $MgSO_4 \cdot H_2O$, $KMgCl_3 \cdot 6H_2O$, and NaCl in 100 cm^3 of water at $T = 25$ °C are 167 g, 71 g, 65 g, and 40 g, respectively.)
(105) Harvie, C. E.; Weare, J. H.; Hardie, L. A.; Eugster, H. P. *Science* **1980**, *208*, 498.
(106) Hanson, D. R.; Ravishankara, A. R.; Solomon, S. *J. Geophys. Res.* **1994**, *99*, 3615.
(107) Kolb, C. E.; Worsnop, D. R.; Zahniser, M. S.; Davidovits, P.; Keyser, L. F.; Leu, M.-T.; Molina, M. J.; Hanson, D. R.; Ravishankara, A. R.; Williams, L. R.; Tolbert, M. A. Laboratory studies of atmospheric heterogeneous chemistry. In *Problems and Progress in Atmospheric Chemistry*; Barker, J. R., Ed.; World Scientific Publishing Company: Singapore, 1995; Vol. 3, p 771.
(108) Kolb, C. E.; Jayne, J. T.; Worsnop, D. R.; Davidovits, P. *Pure Appl. Chem.* **1997**, *69*, 959.
(109) Gebel, M. E.; Finlayson-Pitts, B. J.; Ganske, J. A. *Geophys. Res. Lett.* **2000**, *27*, 887.
(110) Smith, G. D.; Woods, E.; DeForest, C. L.; Baer, T.; Miller, R. E. *J. Phys. Chem. A* **2002**, *106*, 8085.
(111) Ghosal, S.; Hemminger, J. C.; Bluhm, H.; Mun, B. S.; Hebenstreit, E. L. D.; Ketteler, G.; Ogletree, D. F.; Requejo, F. G.; Salmeron, M. *Science* **2005**, *307*, 563.
(112) Jungwirth, P.; Tobias, D. J. *J. Phys. Chem. B* **2001**, *105*, 10468.
(113) Roeselova, M.; Vieceli, J.; Dang, L. X.; Garrett, B. C.; Tobias, D. J. *J. Am. Chem. Soc.* **2004**, *126*, 16308.
(114) Vieceli, J.; Roeselova, M.; Potter, N.; Dang, L. X.; Garrett, B. C.; Tobias, D. J. *J. Phys. Chem. B* **2005**, *109*, 15876.
(115) Davidovits, P.; Kolb, C. E.; Williams, L. R.; Jayne, J. T.; Worsnop, D. R. *Chem. Rev.* **2006**, *106*, 1323.

(116) Morris, J. W.; Davidovits, P.; Jayne, J. T.; Jimenez, J. L.; Shi, Q.; Kolb, C. E.; Worsnop, D. R.; Barney, W. S.; Cass, G. R. *Geophys. Res. Lett.* **2002**, *29*, doi 10.1029/2002GL014692.

(117) Nash, D. G.; Tolocka, M. P.; Baer, T. *Phys. Chem. Chem. Phys.* **2006**, *8* (38), 4468.

(118) Shaka, H.; Robertson, W. H.; Finlayson-Pitts, B. J. *Phys. Chem. Chem. Phys.* **2007**, *9*, 1980.

(119) Ebert, M.; Inerle-Hof, M.; Weinbruch, S. *Atmos. Environ.* **2002**, *36*, 5909.

(120) Wise, M. E.; Biskos, G.; Martin, S. T.; Russell, L. M.; Buseck, P. R. *Aerosol Sci. Technol.* **2005**, *39* (9), 849.

(121) Tang, I. N.; Tridico, A. C.; Fung, K. H. *J. Geophys. Res. Atmos.* **1997**, *102*, 23269.

(122) Tang, I. N.; Fung, K. H. *J. Chem. Phys.* **1997**, *106* (5), 1653.

(123) Clarke, A.; Kapustin, V.; Howell, S.; Moore, K.; Lienert, B.; Masonis, S.; Anderson, T.; Covert, D. *J. Atmos. Ocean. Technol.* **2003**, *20*, 1362.